A Process Model for ITCZ Narrowing under Warming Highlights Clear-Sky Water Vapor Feedbacks and Gross Moist Stability Changes in AMIP Models

FIAZ AHMED[®], ^a J. DAVID NEELIN, ^a SPENCER A. HILL, ^{b,c} KATHLEEN A. SCHIRO, ^d AND HUI SU^{a,e}

^a Department of Atmospheric and Oceanic Sciences, University of California, Los Angeles, Los Angeles, California
^b Program in Atmospheric and Oceanic Sciences, Princeton University, Princeton, New Jersey

^c Lamont-Doherty Earth Observatory, Columbia University, Palisades, New York

(Manuscript received 8 September 2022, in final form 30 January 2023, accepted 27 March 2023)

ABSTRACT: Tropical areas with mean upward motion—and as such the zonal-mean intertropical convergence zone (ITCZ)—are projected to contract under global warming. To understand this process, a simple model based on dry static energy and moisture equations is introduced for zonally symmetric overturning driven by sea surface temperature (SST). Processes governing ascent area fraction and zonal mean precipitation are examined for insight into Atmospheric Model Intercomparison Project (AMIP) simulations. Bulk parameters governing radiative feedbacks and moist static energy transport in the simple model are estimated from the AMIP ensemble. Uniform warming in the simple model produces ascent area contraction and precipitation intensification—similar to observations and climate models. Contributing effects include stronger water vapor radiative feedbacks, weaker cloud-radiative feedbacks, stronger convection-circulation feedbacks, and greater poleward moisture export. The simple model identifies parameters consequential for the inter-AMIPmodel spread; an ensemble generated by perturbing parameters governing shortwave water vapor feedbacks and gross moist stability changes under warming tracks inter-AMIP-model variations with a correlation coefficient ~0.46. The simple model also predicts the multimodel mean changes in tropical ascent area and precipitation with reasonable accuracy. Furthermore, the simple model reproduces relationships among ascent area precipitation, ascent strength, and ascent area fraction observed in AMIP models. A substantial portion of the inter-AMIP-model spread is traced to the spread in how moist static energy and vertical velocity profiles change under warming, which in turn impact the gross moist stability in deep convective regions—highlighting the need for observational constraints on these quantities.

SIGNIFICANCE STATEMENT: A large rainband straddles Earth's tropics. Most, but not all, climate models predict that this rainband will shrink under global warming; a few models predict an expansion of the rainband. To mitigate some of this uncertainty among climate models, we build a simpler model that only contains the essential physics of rainband narrowing. We find several interconnected processes that are important. For climate models, the most important process is the efficiency with which clouds move heat and humidity out of rainy regions. This efficiency varies among climate models and appears to be a primary reason for why climate models do not agree on the rate of rainband narrowing.

KEYWORDS: Intertropical convergence zone; Diagnostics; Idealized models

1. Introduction

The physics of moist convection force cloudy updrafts to occupy smaller areas than subsiding, noncloudy regions (Bjerknes 1938; Bretherton 1987). As a consequence, even on long time scales, regions with vertically deep ascent occupy a small fraction of the tropics (Pierrehumbert 1995). This property also holds for the intertropical convergence zone (ITCZ)—defined here as tropical regions with zonal mean ascent. The meridional width of the ITCZ and the tropical ascent area fraction contract under global warming. This is

Supplemental information related to this paper is available at the Journals Online website: https://doi.org/10.1175/JCLI-D-22-0689.s1.

Corresponding author: Fiaz Ahmed, fiaz@ucla.edu

true in both observations (Wodzicki and Rapp 2016; Byrne et al. 2018; Su et al. 2020) and most climate models (Lau and Kim 2015; Byrne and Schneider 2016b; Su et al. 2017; Donohoe et al. 2019; Schiro et al. 2019, 2022). This contraction holds consequences for regional precipitation trends (Neelin et al. 2006; Chou et al. 2013a) and the global radiative balance (Su et al. 2017).

Climate models exhibit substantial spread in the rate of ascent area change under global warming. Several models even predict ascent area expansion instead of narrowing (Byrne and Schneider 2016b; Su et al. 2019). Atmosphere-only models display comparable spread to coupled atmosphere-ocean models (Su et al. 2019). In the Coupled Model Intercomparison Project phase 6 ensemble (CMIP6; Eyring et al. 2016), the spread in the tropical ascent area change per unit surface warming correlates with the spread in the equilibrium climate sensitivity (Knutti et al. 2017; Sherwood et al. 2020)—likely resulting from teleconnections between the radiative effects

DOI: 10.1175/JCLI-D-22-0689.1

^d Department of Environmental Sciences, University of Virginia, Charlottesville, Virginia

^e Department of Civil and Environmental Engineering, The Hong Kong University of Science and Technology, Clear Water Bay, Hong Kong

of high clouds in the ascent regions and low cloud controlling factors in the descent regions (Schiro et al. 2022). Given its importance for both regional precipitation trends and climate sensitivity estimates, it is imperative to better understand the intermodel spread in the ascent area response to warming.

Tropical ascent area contraction under warming is modulated by a variety of processes. The upped-ante mechanism (Neelin et al. 2003; Chou and Neelin 2004) links ITCZ narrowing to increased horizontal advective drying over the ITCZ margins. Other proposed mechanisms involve the changing gross moist stability in ascent areas (Chou and Neelin 2004; Byrne and Schneider 2016b), cloud-radiative feedbacks (Harrop and Hartmann 2016; Dixit et al. 2018; Albern et al. 2018; Watt-Meyer and Frierson 2019), poleward moisture transports (Byrne and Schneider 2016b; Burls and Fedorov 2017) and reduced seasonal migration range (Donohoe et al. 2019). Many of these impacts can be understood using a diagnostic framework based on thermodynamic constraints (Byrne and Schneider 2016a,b; Jenney et al. 2020). Byrne and Schneider (2016a) link the ascent area fraction to the column moist static energy (MSE) partitioning between ascent and descent areas. This framework, while insightful, requires prior knowledge of ascent and descent area fractions for application, thus providing an implicit solution for the ascent area fraction. In this study, we seek an explicit solution for the ascent area fraction. This solution is sought to obtain a process-level understanding of ascent area narrowing under warming.

Idealized models that drive an overturning circulation with a prescribed thermal forcing (e.g., Raymond 1994; Polvani and Sobel 2002; Bretherton and Sobel 2002; Peters and Bretherton 2005; Bretherton et al. 2006; Kuang 2012; Wofsy and Kuang 2012; Ahmed and Neelin 2019; Emanuel 2019) are relevant to the ascent area fraction problem. Models of this class have simple representations for convection and radiation. Rotational constraints such as angular momentum conservation (Held and Hou 1980) are generally absent. The ascending area of the overturning circulation is internally determined by the model physics. Though simple in construction, such models provide insight into processes coupling convection, circulation and radiation in Hadley and Walker circulations. These include influences on the ITCZ width such as cloud-radiative feedbacks (Bretherton and Sobel 2002), advective drying (Bretherton and Sobel 2002; Emanuel 2019), and surface gustiness feedbacks (Wofsy and Kuang 2012). We use a similar model to study SST-driven meridional overturning circulation in the tropics (as in Ahmed and Neelin 2019). The model physics are primarily governed by constraints of dry and moist static energy conservation. For a given input SST profile, the model predicts the ascent area fraction as well as meridional profiles of column water vapor (CWV) and precipitation (Fig. 1c). Despite quantitative differences in the precipitation rates and CWV values, the simple model qualitatively reproduces the zonal mean structures (Fig. 1b).

The simple model introduced here also proves useful in identifying sources of spread in the ascent area response to warming among complex climate models. For this purpose, an ensemble of Atmospheric Model Intercomparison Project (AMIP) models is used. The use of atmosphere-only models

eliminates the complicating influence of intermodel differences from zonal asymmetries in the SST pattern. The model setup and parameterizations are described in sections 2 and 3, respectively. Analytic expressions for the ascent area fraction and related ascent area properties, and considerations for comparison to realistic-SST cases, are discussed in section 4. Section 5 discusses ways to estimate the simple model parameters using AMIP data. Section 6 explores the response of the simple model to uniform warming. Section 7 uses the simple model results to explore the intermodel spread in the AMIP ensemble. A discussion and summary of the results are provided in section 8.

2. Model setup

a. Steady equations

The steady state column-integrated moisture and temperature equations are given by

$$\langle \nabla \cdot (\overline{\mathbf{v}}\overline{q}) \rangle + [\nabla \cdot \overline{(\mathbf{v}'q')}] = E - P$$
 (1)

$$\langle \overline{\mathbf{v}} \cdot \nabla \overline{T} \rangle + \left\langle \overline{\omega} \frac{\partial \overline{S}}{\partial p} \right\rangle + \left\langle \nabla \cdot \overline{(\mathbf{v}'T')} \right\rangle = F_c + P,$$
 (2)

where \overline{q} and \overline{T} are the time-mean specific humidity and temperature, respectively; \overline{S} is the time-mean dry static energy (DSE); $\overline{\mathbf{v}}$ is the time-mean horizontal velocity vector; $\overline{\boldsymbol{\omega}}$ is the time-mean vertical pressure velocity; and $\langle \dots \rangle$ denotes vertical integration from the surface to the tropopause. The source and sink terms in (1) are the time-mean surface evaporation Eand precipitation P. In (2), F_c is the time-mean net energy input to the atmospheric column including radiative and sensible heat fluxes. The primed variables are deviations from timemean (transient eddies). We have assumed that $\overline{\omega}$ vanishes at the surface and at the tropopause (the rigid lid assumption). The moisture terms $(\overline{q} \text{ and } q')$ in (1) are scaled by the latent heat of vaporization L_{ν} and the dry air heat capacity c_{ρ} to have the same units as \overline{T} (K). The flux terms on the right-hand side of (1) and (2) have units of K kg m⁻² s⁻¹. In subsequent sections, the condition of zonal symmetry is imposed on (1) and (2) to obtain a one-dimensional model—with only meridional variations. For a given surface temperature profile with meridional gradients, this model is solved to obtain explicit expressions for the ascent area fraction.

b. Moist and ascent areas

In deriving the ascent area fraction, it is useful to first define a precipitating area. At fast time scales, tropical precipitation is highly sensitive to the column-integrated moisture content (Bretherton et al. 2004; Neelin et al. 2009; Ahmed and Schumacher 2015; Schiro et al. 2016). As a consequence, heavily precipitating zones in the tropics are approximately bound by a single CWV contour. Figure 1a shows the observed precipitation from the Global Precipitation Climatology project (GPCP; Huffman et al. 1997) and CWV calculated using the ERA5 reanalysis product (Hersbach et al. 2020);

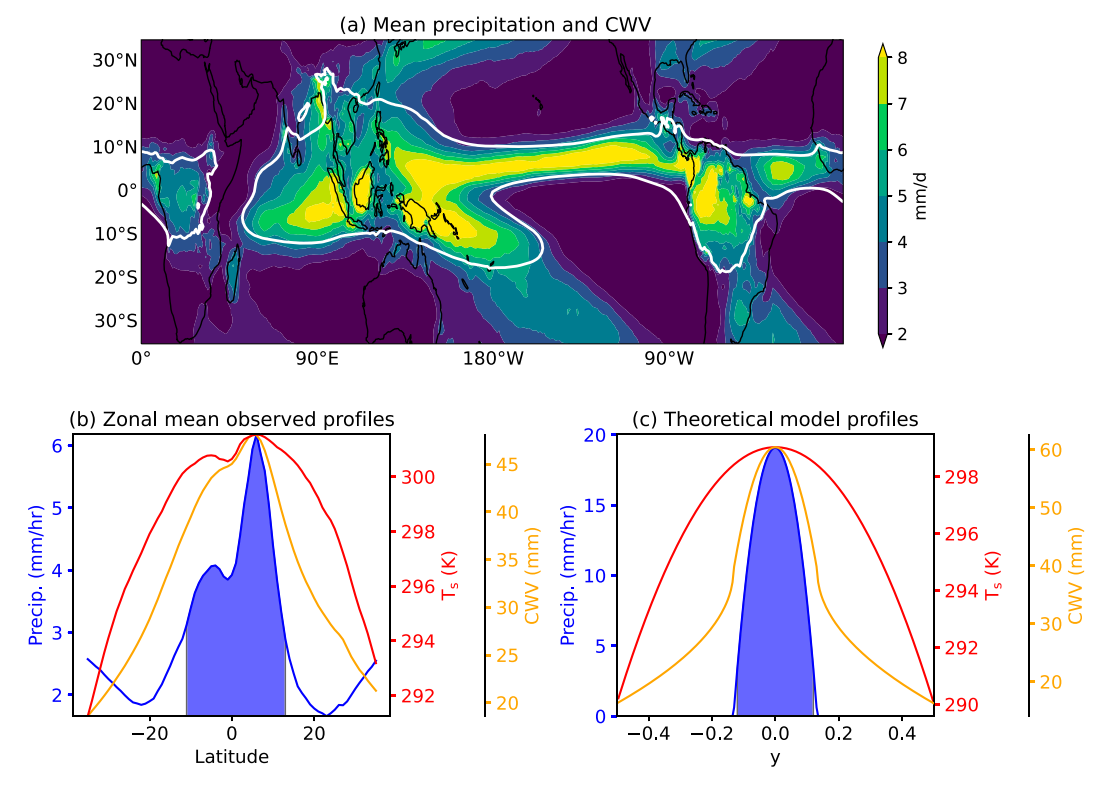


FIG. 1. (a) Mean GPCP precipitation (colors) and the 42.5-mm ERA5 CWV contour (white). (b) Zonal mean profiles of GPCP precipitation (blue), and ERA5 surface temperature T_s (red) and CWV (orange). The blue shading shows the ERA5 zonal mean ascent region. (c) As in (b), but for profiles from the simple model.

both these fields are monthly-mean values averaged over the years 2000–20. Tropical precipitation in Fig. 1a appears nearly bound by a single CWV value. This observed property is now used to define an idealized *moist area* as the region bound by a CWV value separating the precipitating and nonprecipitating regions. In our idealized setup, the moist area is equivalent to the precipitating area. Figure 1a suggests that this equivalence holds approximately in the tropics; deviations associated with frontal precipitation appear in the subtropics.

The ascent area is defined as the region with vertical velocity at some predefined level less than zero. When applying this definition to reanalysis or climate model data, we consider vertical velocity at the 500-hPa level (ω_{500}). In the simple model, vertical truncation provides a natural measure with which to define the ascent area (section 2c). Note that the precipitating and ascent areas are closely related, but not necessarily equivalent, since regions with weak descent can also be precipitating. This is clearly seen in Fig. 1b, where the zonal mean ascent area appears as a subset of the moist, precipitating area.

The moist and ascent region areas are denoted A_m and A_a , respectively. The total domain area under consideration is A_T . The latitudinal extent of the domain is assumed to extend to the edge of the Hadley cell (\sim 35°N–35°S). We now define integral operators over the moist area, the ascent area, and the total domain:

$$\{...\}_{m} = \frac{1}{A_{T}} \iint_{A_{m}} ... dx \, dy,$$
 (3)

$$\{...\}_a = \frac{1}{A_T} \iint_{A_a} ... dx \, dy,$$
 (4)

$$\{...\} = \frac{1}{A_T} \iint_{A_T} ... dx \, dy.$$
 (5)

Note that (3)–(5) are normalized by A_T . Zonal symmetry is assumed, so a single meridional coordinate is sufficient to measure horizontal distances. The domain is described by fractional y coordinates, with y=0 at the equator and $y=\pm 1/2$ at the northern and southern boundaries, respectively (Fig. 1c). The fractional coordinates have the advantage of being agnostic to changes in the domain area A_T that could result, for instance, from Hadley cell widening (Lau and Kim 2015). The terms equator and northern and southern boundaries are only used in a nominal sense since rotational constraints are absent in our setup.

c. Balances at the equator

It is assumed that the precipitation peaks at y = 0 and corresponds to the SST peak. Meridional symmetry is assumed, which implies that the mean meridional divergent wind at the equator (y = 0) vanishes. This eliminates the meridional

moisture advection term from (1). Since zonal symmetry does not permit zonal moisture gradients, the zonal moisture advection term also drops out. The weak temperature gradient assumption (WTG; Sobel and Bretherton 2000; Sobel et al. 2001) is assumed at y = 0, which eliminates both the temperature advection and eddy transport terms from (2). Furthermore, the eddy moisture transports at y = 0 are neglected since downgradient moisture transport in the deep tropics is small (Trenberth and Stepaniak 2003)—although including this term can have consequences for the ITCZ width (Sobel and Neelin 2006). Tropical convection also imposes strong leading-order constraints on the vertical structures of the wind and thermodynamic fields (Emanuel et al. 1994; Neelin and Yu 1994). We therefore assume fixed vertical structures for the horizontal and vertical winds, as well as fixed structures for the DSE and moisture (see Neelin and Zeng 2000 for more details). These assumptions introduce M_{q0} and M_{s0} , which are the gross moisture stratification and gross dry stability, respectively (Yu et al. 1998; Chou et al. 2013b), at y = 0, and have the following definitions:

$$M_{s0} = -\left(\Omega \frac{\partial \overline{S}}{\partial p}\right),\tag{6}$$

$$M_{q0} = \left(\Omega \frac{\partial \overline{q}}{\partial p}\right). \tag{7}$$

In (6) and (7), Ω is nondimensional and denotes a fixed vertical structure for the vertical velocity such that

$$\omega(y, p) = \omega_1(y)\Omega(p). \tag{8}$$

Note that even though Ω is fixed in space, it is free to vary with climate and can capture, for instance, the increasingly top-heavy vertical profiles in a warmer world (Neogi and Singh 2022). With the above assumptions, the thermodynamic equations (1) and (2) at y = 0 reduce to

$$M_{a0}\omega_1 = E_0 - P_0, (9)$$

$$-\omega_1 M_{s0} = F_{c0} + P_0, \tag{10}$$

where ω_1 is the strength of the vertical velocity, and E_0 , P_0 , and F_{c0} are the surface evaporation, precipitation, and net column energy input, respectively, at y=0. Note that $M_{q0}\omega_1$ in (9) and $-\omega_1 M_{s0}$ in (10) represent the column-integrated vertical moisture and DSE divergence, respectively. Eliminating ω_1 from (9) and (10) gives

$$m_0 = \frac{E_0 + F_{c0}}{P_0 + F_{c0}}. (11)$$

In (11), m_0 is the relative gross moist stability at y = 0:

$$m_0 = \frac{M_{s0} - M_{q0}}{M_{s0}}. (12)$$

The parameter defined in (12) measures the efficiency of column MSE export by convection (Neelin and Held 1987;

Raymond et al. 2009). The relative gross moist stability m_0 depends on the vertical structures of MSE, DSE and vertical velocity (Ω), as well as the tropopause height—the latter controls the upper limit of the vertical integration in M_{s0} and M_{q0} . The expression (11) thus equates the ratio between column-integrated MSE and DSE sources to the gross moist stability, and is analogous to the energetic constraint derived in Byrne and Schneider (2016a). Note that this is the key equation that provides subsequent expressions for the moist and ascent area fractions.

d. Domain-mean energy balances

Using the domain-mean operator—defined in (5)—on (2) gives

$$\{P\} = \{P\}_m = -\{F_c\} + f_T, \tag{13}$$

where f_T represents the poleward DSE export at the domain boundary $(y = \pm 1/2)$. When poleward transports are neglected, (13) reduces to a statement of domain-wide radiative convective equilibrium. In equating $\{P\}$ to $\{P\}_m$, precipitation is assumed to occur only in the moist region following arguments in section 2b. The domain-mean evaporation is inferred using (1) and (13):

$$\{E\} = \{P\} + f_q = -\{F_c\} + f_T + f_q, \tag{14}$$

where f_q represents the poleward moisture export at $y = \pm 1/2$.

e. Idealized profiles

To obtain explicit expressions for ascent area properties from (11), it is necessary to assume functional forms for the surface temperature and CWV. Surface temperature T_s is assumed to follow:

$$T_{s}(y) = T_{0} - 3\sigma_{T}y^{2},$$
 (15)

where σ_T controls the meridional gradient of surface temperature. The expression in (15) assumes that SST maximizes at a value T_0 at the equator and decreases with latitude.

The CWV is denoted by q, and its meridional distribution is characterized by a threshold value $q_{\rm in}$. Figure 1a shows that much of the ITCZ region is bound by a single CWV value. We take the limit of this observed relationship to assume that *all* the precipitation in the domain occurs for CWV values greater than a threshold value $q_{\rm in}$. As a result, $q_{\rm in}$ effectively marks the interface between precipitating and nonprecipitating regimes. The fractional width of the moist area is y_m , which is an unknown to be determined. Meridional symmetry ensures that the moist area extends from $-y_m/2$ to $y_m/2$. The functional form for q(y) in the moist and dry regions is assumed to be

$$q(y) = \begin{cases} q_0 - 3\sigma_m y^2, & |y| \le \frac{y_m}{2} \text{(moist region)} \\ q_{in} - \frac{3\sigma_d}{2} \sqrt{|y| - \frac{y_m}{2}}, & |y| > \frac{y_m}{2} \text{(dry region)} \end{cases}$$
(16)

The equatorial CWV value is q_0 and that at the moist-dry interface ($|y| = y_m/2$) is q_{in} . Both q_0 and q_{in} depend on T_0 .

Specifically, they are determined by constant column relative humidity values r_0 and r_{in} . These fractions are applied to the saturation column water vapor along a moist adiabat with surface temperature T_0 . The CWV gradients in the moist and dry regions are controlled by σ_m and σ_d , respectively. In the moist region, CWV decays quadratically like the SST profile in (15). In the dry domain, the CWV profile decays sublinearly $\propto \sqrt{y}$. The choice of different decay scales for CWV in the moist and dry regimes is motivated by the fact that circulation can introduce substantial differences between the dry and moist regime CWV structures (see supplemental material). These different scalings are seen in Fig. 1b, where the ERA5 zonal mean CWV field switches from a concave function near the equator to a convex function in the subtropics. We further demand that $q = q_d$ at the domain boundary, where |y| = 1/2. The surface temperature at the domain boundary is T_d , which is computed using $y = \pm 1/2$ in (15). A moist adiabat with surface temperature T_d is used to compute a saturation CWV value, which then multiplies a constant column relative humidity at the domain boundary (r_d) to determine q_d . Section 5 discusses the numerical estimation for r_0 , r_{in} and r_d in more detail. In reality, the functional form for CWV is determined by dynamical balances (see supplemental material), but it is externally imposed here to simplify the analytic treatment.

Using the constraint that $q = q_{\text{in}}$ at $|y| = y_m/2$, and $q = q_d$ at |y| = 1/2 allows us to determine σ_m and σ_d :

$$\sigma_m = \frac{q_0 - q_{\rm in}}{3} \left(\frac{y_m}{2} \right)^{-2},\tag{17}$$

$$\sigma_d = \frac{2(q_{\rm in} - q_d)}{3} \left(\frac{1}{2} - \frac{y_m}{2}\right)^{-0.5}.$$
 (18)

Clearly, the CWV gradients in the moist and dry regions are functions of y_m . Figure 1c shows the typical shapes of T_s and CWV, with the separation between the moist precipitating and dry nonprecipitating regimes evident in the CWV profile. In the simple process model, the CWV field translates SST gradients into an overturning circulation. Although several aspects of the CWV field are externally imposed, the width of the precipitating zone y_m is left unspecified to be determined by interactions between convection, radiation, and circulation.

3. Parameterizations

This section presents physically motivated parameterizations for different mechanisms operating in the simple model. A number of parameters are introduced as a result. Numerical estimation of these parameters is deferred until section 5, and only the analytical forms are discussed here.

a. Atmospheric heating

The atmospheric heating term F_c is decomposed into three subterms:

$$F_c = F_0 + F_P + F_a. (19)$$

In (19), F_0 is a spatially uniform atmospheric heating term. This parameter has a fixed value of -80 W m^{-2} , chosen such

that the domain-mean precipitation in the simple model is close to the AMIP multimodel mean. This parameter has minimal impact on our results and is not perturbed in any experiments. If the spatial structure in sensible heat fluxes is ignored, a uniform sensible heat flux can also be included in F_0 .

Terms F_P and F_q are contributions to atmospheric heating due to variations in precipitation and CWV, respectively. Term F_P is parameterized using

$$F_P = r_c P. (20)$$

In (20), the parameter r_c is positive and represents cloudradiative effects as a constant fraction of the precipitation. This simple parameterization is well established (Su and Neelin 2002; Bretherton et al. 2005; Peters and Bretherton 2005; Kim et al. 2015; Adames and Kim 2016). Physically, this parameter measures the tropospheric radiative heating per unit precipitation due to longwave trapping by deep convective clouds, as well as associated cirrus and anvil clouds.

The term F_q is parameterized using

$$F_{q} = \begin{cases} r_{qm}q, & q \ge q_{\text{in}}(\text{moist region}) \\ r_{qd}q, & q < q_{\text{in}} \text{ (dry region)} \end{cases}$$
 (21)

In (21), the clear-sky radiative effects of water vapor are assumed to have different effects in the moist and dry regions. Shortwave absorption of water vapor heats the troposphere in all environments (Donohoe et al. 2014; Paynter and Ramaswamy 2014; DeAngelis et al. 2015), but the longwave effects are subtler (Pendergrass and Hartmann 2014; Emanuel et al. 2014; Beucler and Cronin 2016). Specifically, increasing water vapor in dry conditions acts as a tropospheric energy sink (by increasing radiation to the surface), but heats the column in moist conditions. The latter effect is more pronounced if water vapor increases preferentially in the free troposphere than the boundary layer (Beucler and Cronin 2016). We therefore use two different values r_{am} and r_{qd} to represent contrasting clear-sky water vapor feedbacks in the moist and dry regimes, respectively. Here $r_{qm} > 0$ and $r_{qd} < 0$. Parameter estimation using AMIP models in section 5 further supports the choice of parameterization in (21). Note that in (21), the CWV value where the F_q dependence on water vapor switches sign is assumed to occur at the precipitating interface $(q = q_{in})$. Although a different CWV value can be used to mark this switch, $q_{\rm in}$ is retained for ease of analytic treatment.

b. Evaporation

Meridional variations in surface evaporation are smaller when compared to precipitation (e.g., Siler et al. 2018). We assume a constant surface evaporation in the domain $(E = E_0)$, and write

$${E} = E_0; {E}_m = E_0 y_m.$$
 (22)

c. Poleward transports

The poleward DSE export is assumed to occur down the meridional surface temperature gradient, following traditional diffusive assumptions in energy balance models (e.g., North 1975):

$$f_T = D_T \frac{dT_s}{dy} \bigg|_{y=\pm 1/2} = 3D_T \sigma_T, \tag{23}$$

where D_T is a diffusion coefficient for DSE export with units of W m⁻² K⁻¹. The surface temperature gradient at $y = \pm 1/2$ is computed using (15) and yields (23). Following the approach in moist energy balance models (Frierson et al. 2007; Hwang and Frierson 2010; Siler et al. 2018; Armour et al. 2019), poleward moisture transports are parameterized using the near surface specific humidity gradient at the domain boundary:

$$f_q = D_q 0.8 \left. \frac{dq^*}{dy} \right|_{v=\pm 1/2} = 0.8 \left[\frac{L_v q^*(T_d)}{R_u T_d^2} \right] 3D_q \sigma_T.$$
 (24)

In (24), $q^*(T_d)$ is the near-surface saturation specific humidity at the domain boundary ($y=\pm 1/2$). The near-surface relative humidity at the domain boundary is assumed to be 80% following Hwang and Frierson (2010), which introduces the factor of 0.8 in (24). Note that this factor is distinct from the *column* relative humidity r_d introduced in section 2e. The parameter D_q is the moisture diffusion coefficient. The term inside the square brackets in (24) appears upon applying the Clausius–Clapeyron (CC) relationship, and R_v is the water vapor gas constant. Moist energy balance models generally use (24) to parameterize MSE transports; we use (24) to parameterize moisture transports alone, since our approach requires separating the poleward moisture and DSE transports.

d. Precipitation

The observed dependence of precipitation on CWV (Bretherton et al. 2004; Neelin et al. 2009) suggests a parameterization with a nonlinear CWV dependence:

$$P(q) = \begin{cases} \alpha_m (q - q_{\rm in}), & q > q_{\rm in} \\ 0, & q \le q_{\rm in}, \end{cases}$$
 (25)

where α_m controls the precipitation strength per unit CWV increase above $q_{\rm in}$. At fast time scales $q_{\rm in}$ is governed by the degree of entrainment (Kuo et al. 2017). However, at longer time scales, $q_{\rm in}$ is also impacted by the fraction of time spent in the nonprecipitating regime (Ahmed et al. 2020). The parameter α_m is not prescribed, but is determined by the energetic constraint (13) and parameterizations (19)–(20). These constraints yield

$$\alpha_m = \left(\frac{3}{2}\right) \frac{f_T - \{F_0 + F_q\}}{(q_0 - q_{\rm in})(1 + r_c)} \frac{1}{y_m}.$$
 (26)

e. Temperature dependence

The gross moist stability m_0 and the cloud-radiative feedback parameter r_c are expected to be sensitive to climate. Ascent area gross moist stability changes under warming (Peters and Bretherton 2005; Chou et al. 2013b; Wills et al. 2017),

although the sign of this change is unclear. The uncertainty comes from the two components of m_0 : the gross dry stability M_{s0} and gross moisture stratification M_{q0} . These quantities are both expected to increase under warming, but for different reasons (Chou and Neelin 2004; Chou et al. 2013b). The gross moisture stratification increases due to near-constant relative humidity with warming, which steepens the vertical moisture gradient. The gross dry stability primarily increases because of the tropopause rise, which allows greater DSE export out of the column. These two processes are separately parameterized using the following power law dependence on T_0 :

$$M_{s0} = M_{\rm sref} \left(\frac{T_0}{T_{\rm ref}} \right)^{\gamma_s}, \tag{27}$$

$$M_{q0} = M_{\text{qref}} \left(\frac{T_0}{T_{\text{ref}}} \right)^{\gamma_q}. \tag{28}$$

The cloud-radiative feedback parameter r_c is also expected to decrease with warming, because convective clouds would detrain fewer anvil clouds (Bony et al. 2016) and therefore trap lesser longwave heating. This temperature dependence for r_c is validated using AMIP model data in section 5. Expressions similar to (27) and (28) are used to parameterize this effect:

$$r_c = r_{\text{cref}} \left(\frac{T_0}{T_{\text{ref}}} \right)^{\gamma_r}. \tag{29}$$

In (27)–(29), power law formulations—as opposed to linear formulations—ensure that these parameters do not take negative unphysical values under large temperature changes explored in section 6. Parameters γ_s , γ_q , and γ_r control the rate at which M_{s0} , M_{q0} , and r_c , respectively, vary with T_0 . A reference temperature $T_{\rm ref}$ coincides with reference values $M_{\rm sref}$, $M_{\rm qref}$, and $r_{\rm cref}$.

4. Moist and ascent area properties

a. Moist area fraction

We now define the effective gross moist stability m_{eff} :

$$m_{\rm eff} = m_0 (1 + r_c) - r_c. (30)$$

This parameter combines the effects of the gross moist stability m_0 and the cloud-radiative feedback strength r_c . The parameter $m_{\rm eff}$ is critical in theories for both steady overturning circulations (e.g., Su and Neelin 2002; Bretherton and Sobel 2002) and tropical variability (e.g., Adames and Kim 2016; Ahmed 2021).

Next, we note using (16) that CWV integrated over the moist and dry regimes respectively yields

$$\{q\}_m = \beta_m y_m,\tag{31}$$

$$\{q\}_d = \beta_d (1 - y_m),$$
 (32)

where

$$\beta_m = \frac{2q_0 + q_{\rm in}}{3},\tag{33}$$

$$\beta_d = \frac{q_{\rm in} + 2q_d}{3}.\tag{34}$$

Using the energetic constraint (14), the evaporation parameterization (22) and expressions (31)–(34) allows us to write the domain mean evaporation E_0 as

$$E_0 = \frac{f_h - F_0 - r_{qd}\beta_d}{1 + r_c} - \frac{C_0}{1 + r_c} y_m,$$
 (35)

where

$$C_0 = r_{am}\beta_m - r_{ad}\beta_d. (36)$$

In (35) we have defined $f_h = f_T + f_q(1 + r_c)$ as a measure of poleward MSE transport. Now, the meridional profiles for T_s and CWV from (15) and (16), the parameterizations from section 3 and the expression for E_0 from (35) are used in (11) to obtain a quadratic equation in the moist area fraction y_m :

$$C_0 y_m^2 + C_1 y_m + C_2 = 0, (37)$$

where

$$C_1 = r_{qd}\beta_d - f_h - (1 - m_{\text{eff}})r_{qm}q_0 + m_{\text{eff}}\left(F_0 - \frac{3}{2}C_0\right),$$
(38)

$$C_2 = \frac{3m_{\text{eff}}}{2} (f_T - F_0 - r_{qd}\beta_d). \tag{39}$$

Solutions to the quadratic in (37) yield values for the moist area fraction y_m as functions of the T_s profile, parameters controlling the circulation and radiative feedbacks, and poleward transports.

A linear approximation to (37) is now derived by neglecting the y_m dependence—the second term on the right-hand side—in (35). This is tantamount to neglecting the clear-sky radiative effects from the moist area *only* when inferring E_0 using energetic constraints. Following this approximation, y_m is approximated by

$$y_m \approx -C_2/C_1. \tag{40}$$

The expression (40) can also be motivated by neglecting the quadratic term in (37) following the small y_m limit.

b. Ascent area properties

The ascent area in the simple model is defined as the region with upward vertical motion, that is, $\omega_1 < 0$. The ascent area is assumed to extend from $-y_a/2$ to $y_a/2$, giving the ascent area fraction y_a . Since y_a defines the boundary between ascent and descent regions, it follows that $\omega_1 = 0$ at $y = \pm y_a/2$. This condition of zero ascent applied to the DSE equation (2)

implies that the precipitation must exactly balance the atmospheric cooling at $|y| = y_a/2$:

$$P + F_c = 0$$
 at $y = \pm \frac{y_a}{2}$. (41)

The expression (41) also assumes WTG at the region of zero ascent. Note that $|y_a| < |y_m|$ since (41) cannot be satisfied in nonprecipitating regions (except for the pathological case with $F_c = 0$). Using the functional form for q from (16), the parameterizations for precipitation (25) and atmospheric heating (19)–(21) in (41) yields an expression for y_a in terms of y_m :

$$y_a = y_m \sqrt{\frac{F_0 + r_{qm}q_0 + \alpha_m (1 + r_c)(q_0 - q_{in})}{[r_{qm} + \alpha_m (1 + r_c)](q_0 - q_{in})}}.$$
 (42)

The ascent area fraction derived in (42) is closely related to the ascent strength (Byrne and Schneider 2016a; Su et al. 2019; Schiro et al. 2019). We now derive expressions that make this relationship clearer and allow comparison to similar relationships in climate models. We first derive the ascent area averaged precipitation using (25):

$$P_a = \frac{\{P\}_a}{y_a} = \alpha_m [q_0 - q_{\rm in}] \left[1 - \frac{1}{3} \left(\frac{y_a}{y_m} \right)^2 \right], \tag{43}$$

which can be solved using the expression for α_m from (26) and that for y_a from (42). To derive expressions for the strength of the ascending and descending motions, we average the DSE energy budget (2) over the ascent region, use the WTG approximation, (6) and (8) to get

$$-M_{s0}\{\omega_1\}_a = \{P + F_c\}_a,\tag{44}$$

where M_{s0} is assumed to be constant over the precipitating region following Chou et al. (2013b). Now writing $\{\omega_1\}_a = \omega_a y_a$ in (44) yields

$$\omega_a = -\left(\frac{F_{ca} + P_a}{M_{s0}}\right),\tag{45}$$

where ω_a measures the ascent strength and $F_{ca} = \{F\}_a/y_a$. The numerator in (45) is computed using the atmospheric heating parameterization in (19), the expression for y_a from (42) and the ascent area averaged precipitation from (43). This provides the following expression for ω_a :

$$\omega_a = -\frac{2}{3} \frac{[F_0 + r_{qm}q_0 + \alpha_m(1 + r_c)(q_0 - q_{\rm in})]}{M_{s0}}.$$
 (46)

Since α_m contains an inverse dependence on y_m —from (26)—it follows using (42) that the ascent area strength is inversely related to the ascent area fraction.

To obtain the descent strength, the DSE balance in (2) is averaged over the descent region—denoted by the operator $\{\ldots\}_{ds}$ —and combined with the domain energy balance (13) to yield

TABLE 1. Reference parameter values for the control experiment.

Parameter	Description	Value	Units
T_0	Peak temperature	299.03	K
σ_T	Meridional temperature gradient parameter	12	K
M_{s0}	Gross dry stability in peak ascent region	0.34	$\mathrm{K}\;\mathrm{m}^{-1}\;\mathrm{s}^2$
M_{q0}	Gross moisture stratification in peak ascent region	0.25	$\mathrm{K}\;\mathrm{m}^{-1}\;\mathrm{s}^2$
M_{sd0}	Gross dry stability averaged over descent region	0.30	$\mathrm{K}\;\mathrm{m}^{-1}\;\mathrm{s}^2$
D_T	Coefficient of poleward DSE export	0.48	${ m W} { m m}^{-2} { m K}^{-1}$
D_q	Coefficient of poleward moisture export	1.76	${ m W} { m m}^{-2} { m K}^{-1}$
F_0	Spatially uniform atmospheric heating	-80	$\mathrm{W}~\mathrm{m}^{-2}$
r_{qm}	Moist radiative feedback parameter	0.49	$\mathrm{W}~\mathrm{m}^{-2}~\mathrm{mm}^{-1}$
r_{qd}	Dry radiative feedback parameter	-1.23	$\mathrm{W}~\mathrm{m}^{-2}~\mathrm{mm}^{-1}$
r_c	Cloud-radiative feedback parameter	0.14	_
γ_s	Temperature sensitivity of M_{s0}	13.14	_
γ_q	Temperature sensitivity of M_{a0}	13.88	_
γ_r	Temperature sensitivity of r_c	-16.95	_
r_0	Column relative humidity at $y = 0$	0.95	_
$r_{\rm in}$	Threshold column relative humidity for precipitation	0.65	_
r_e	Domain boundary column relative humidity	0.45	_
q_0	Peak CWV value	59.98	mm
$q_{\rm in}$	Threshold CWV value for precipitation	40.72	mm
q_d	Domain boundary CWV value	16.20	mm
c_p	Specific heat capacity of dry air	1004	$\mathrm{J~kg}^{-1}$
$\stackrel{r}{L}_{v}$	Latent heat of vaporization of water	2.26×10^{6}	$J kg^{-1} K^{-1}$
R_v	Gas constant of water vapor	461	$J kg^{-1} K^{-1}$

$$\omega_d = -\omega_a \frac{M_{s0} y_a}{M_{sd} (1 - y_a)} + \frac{\{\langle \mathbf{v} \cdot \nabla T \rangle\}_{ds}}{M_{sd} (1 - y_a)}, \tag{47}$$

where M_{sd} is the gross dry stability averaged over the descent region, defined such that it is a positive quantity. This parameter also has T_0 dependence, which is parameterized using the same formulation as in (27), but with reference value M_{sd0} (see Table 1). The first term on the right-hand side of (47) is the descent strength if WTG were applicable throughout the domain, and is equivalent to the expression used in Su et al. (2019). The second term is the additional descent required to balance horizontal temperature advection in the descent region. In practice, WTG can be applied even in the subtropics (Wood and Bretherton 2006). The contribution from the temperature advection, when averaged over the dry domain, is therefore expected to be smaller. In subsequent discussions, only the WTG estimate of the descent strength from (47) is presented.

c. Considerations for comparison to realistic-SST cases

The model derivation above leverages the zonally symmetric assumption for simplicity. The expressions from (37)–(42) would be more useful if they provide insight into model simulations with realistic SST, including zonal asymmetries. We briefly outline arguments for potential utility, caveats, and metrics when translating the simple model predictions to realistic-SST cases. The most obvious argument for the use of zonal symmetry is that latitudinal variation is the leading spatial dependence in the climate system. A consideration for taking zonal asymmetries into account is that the basic thermodynamic equations (1) and (2) of the model hold for latitudinal and zonal circulations. In realistic-geometry models, integrated quantities, for example over ascent area (4), are

thus postulated to yield better dynamical correspondence to the theoretical model than a simple zonal average. Fractional ascent area changes in the realistic models will thus be compared to its simple-model counterpart $(1/y_a)dy_a/dT_0$, and similarly for fractional changes in ascent strength, domain-mean precipitation and ascent area averaged precipitation.

To see the caveats on the comparison between the simple and realistic models, consider the requirements to introduce zonal asymmetry into our framework. These will involve either assuming that the functional form postulates (15) and (16) hold on sufficiently simple inflow trajectories, or replacing the coefficients based on these postulates in (33) and (34) and (36)–(39) with empirical ascent/descent region averages. A further assumption of negligible net transport by the rotational flow across the ascent/descent boundary would be required, implying sufficiently small variations of q_{in} . Alternately, the model (1) and (2) can be run numerically (using parameterizations from section 3) with realistic SST, although this setup will lack effects from angular momentum conservation. Overall, the analytic results here should represent feedbacks involving the convergent flow sufficiently well to guide the analysis of atmospheric components in full climate models. We restrict our analysis to a collection of AMIP models, to avoid potential effects of differences in the SST pattern of warming on ascent area properties (e.g., Zhou et al. 2019). Over the historical period, most AMIP models display discernible trends in both warming and ascent area properties (Su et al. 2019), and are therefore well suited for our purpose.

5. Parameter estimation

In this section, we briefly discuss the methods used to estimate the simple process model parameters using climate

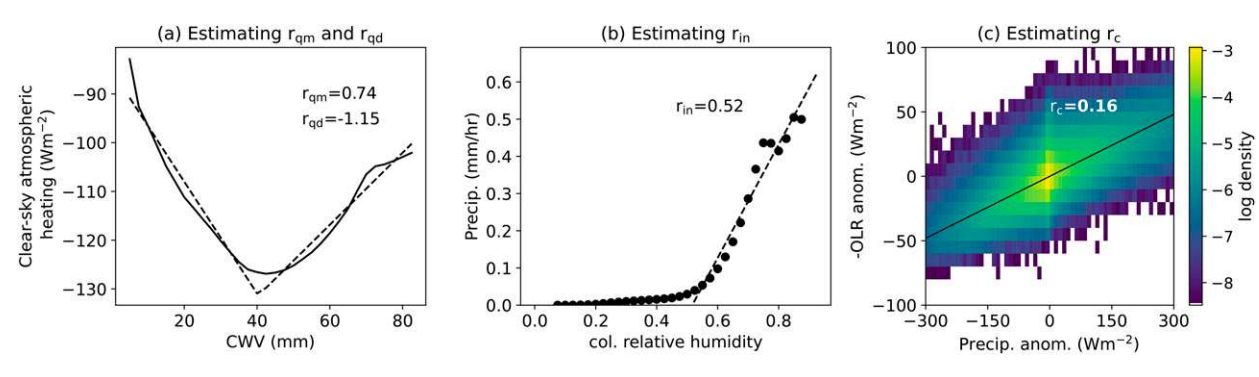


FIG. 2. Parameter estimation for (a) clear-sky water vapor feedbacks r_{qm} and r_{qd} , (b) precipitation onset r_{in} , and (c) cloud-radiative feedbacks r_c using an example AMIP model MPI-ESM1-2-LR. The correlation coefficient for the linear fit in (c) is 0.70.

model data. A set of 29 AMIP models over the historical period (1979–2014) from CMIP6 were selected based on data availability (see the supplemental material for a full list). We use monthly mean AMIP variables for the parameter estimation. The AMIP analysis is limited to 35°N–35°S to match the tropical domain assumption in the simple model. Note that the parameters estimated here are interpreted as bulk quantities that map complex climate model parameterizations onto the simple process model.

a. Surface temperature

The peak surface temperature T_0 is estimated from the AMIP models as the surface temperature averaged over intensely convective regions. These are defined as tropical regions with monthly mean ω_{500} less than the 10th percentile of values at each time step. This definition establishes an analogy between the peak ascent in the simple process model (section 2c) and that in climate models. The results are weakly sensitive to other percentile choices between 5 and 10. The 10th percentile was chosen to ensure adequate sampling for the averaging, particularly when using coarse resolution models.

b. Poleward transport parameters

For each AMIP model, the poleward DSE export (f_T) is computed as the difference between tropics-mean precipitation and net atmospheric cooling including surface sensible heat fluxes. The poleward moisture transport (f_q) is computed as the difference between tropics-mean evaporation and precipitation. The expressions in (23) and (24) are then used to estimate D_T and D_q , respectively. Since all the AMIP models have nearly the same surface temperature pattern, the meridional gradient of surface temperature σ_T is fixed at a value of 12 K when estimating D_q and D_T . This value for σ_T closely fits the AMIP zonal mean surface temperature profile to the profile described by (15).

c. Clear-sky water vapor feedback parameters

The clear-sky water vapor feedback parameters r_{qm} and r_{qd} are estimated by first binning the clear-sky atmospheric cooling against CWV (Fig. 2a). This produces a curve with non-monotonic dependence on CWV. The atmospheric cools more with increasing CWV up until a particular CWV value

(~40 mm in Fig. 2a), beyond which the net atmospheric heating increases with CWV. This behavior is consistent with the results from Beucler and Cronin (2016), as well as the assumptions in (21)—where the clear-sky water vapor feedback parameters were assumed to have different signs in the dry and moist regimes. The slopes of the CWV versus clear-sky cooling in Fig. 2a are estimated through a piecewise linear regression. This yields a positive value for the moist radiative feedback parameter r_{qm} and a negative value for the dry radiative feedback parameter r_{qd} .

d. Gross moist stability and its temperature dependence

To compute m_0 over the peak ascent area, we first compute M_{s0} and M_{q0} over the peak ascent area using their definitions in (6) and (7). Similar to T_0 estimation, we use areas with monthly ω_{500} values less than the 10th percentile. The vertical structure Ω used in (6) and (7) is computed by dividing the vertical profile of ω by ω_{500} . The definition (12) is then used to compute m_0 using M_{s0} and M_{q0} . To estimate γ_s and γ_q from (27) and (28), respectively, we first divide the AMIP historical period (1979–2014) into two subperiods: early historical (1979–96) and late historical (1997–2014). To estimate γ_s , the fractional change in M_{s0} between the late and early historical periods is normalized by the T_0 change between the two periods. This quantity (units of K^{-1}) is termed δ_M , which is then used to estimate γ_s using

$$\gamma_s = \delta_M T_{\text{ref}},\tag{48}$$

where T_{ref} is taken to be the T_0 value in the early historical period. The relationship in (48) is derived from the parameterization in (27). A similar procedure is employed to estimate γ_q using the fractional change in M_{q0} .

e. Cloud-radiative feedback strength and its temperature dependence

Following Kim et al. (2015), the cloud-radiative feedback parameter r_c is computed as the linear regression slope between monthly anomalies of precipitation and negative outgoing longwave radiation (Fig. 2c). For almost all AMIP models examined, we find that this ratio reduces as the tropical mean surface temperature increases. This reduction is parameterized using γ_{rc} in (29), and is estimated similarly to γ_s and γ_q , using the fractional change in r_c ; the one exception is that the

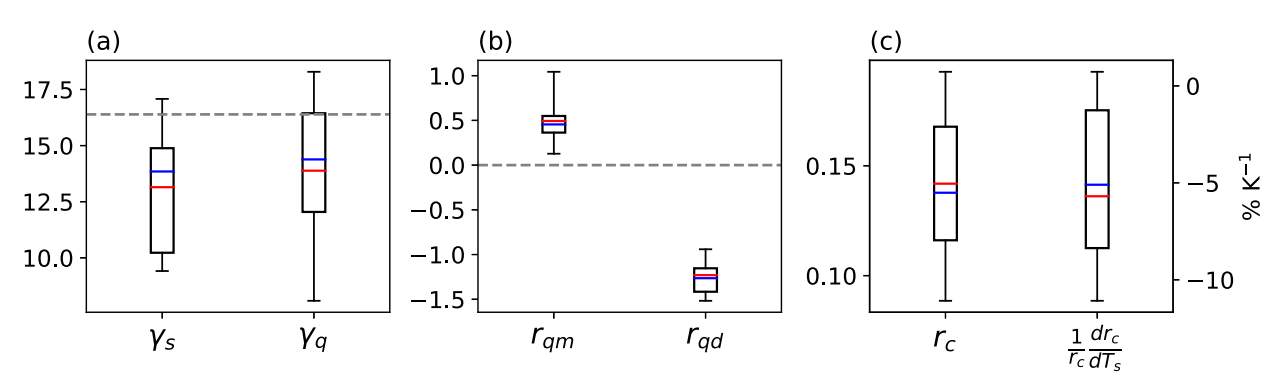


FIG. 3. Model spread among AMIP models in (a) γ_s and γ_q , (b) r_{qm} and r_{qd} , and (c) r_c (left axis) and fractional change in r_c (right axis). The dashed horizontal line in (a) denotes the change implied by CC scaling. The dashed horizontal line in (b) is the zero line that separates r_{qm} and r_{qd} . In each boxplot, the red and blue lines denote the mean and median, respectively.

tropics-mean surface temperature is used instead of T_0 . This reflects the fact that r_c represents cloud-radiative feedbacks over the entire tropical domain, and not solely over the peak ascent region.

f. Column water vapor values q_0 and q_{in}

To estimate q_{in} , we first bin precipitation by the column relative humidity (as in Bretherton et al. 2004; Ahmed and Schumacher 2015; Wolding et al. 2020). This binning procedure yields a strong precipitation increase for binned column relative humidity greater than an apparent threshold value r_{in} . This column relative humidity threshold changes only weakly under global warming (Sahany et al. 2014) and is thus assumed invariant across climates. As shown in Fig. 3b, a linear fit is then applied to the strongly precipitating portion of the binned curve. The x intercept of this linear fit yields r_{in} . For example, for the model shown in Fig. 2b, $r_{\rm in} = 0.52$. Using $r_{\rm in}$, we then estimate $q_{in} = r_{in}q_0^*$, where q_0^* is the saturation column water vapor computed along a moist adiabat with surface temperature T_0 and surface pressure 1000 hPa. Using T_0 to estimate $r_{\rm in}$ reflects the fact that under WTG, the free-tropospheric temperature profile that determines $r_{\rm in}$ is predominantly controlled by T_0 . The peak column relative humidity r_0 is the maximum monthly mean column relative humidity. Using r_0 , we estimate $q_0 = r_0 q_0^*$.

Figure 3 shows the spread in select AMIP model parameters. The parameters γ_s and γ_q , which control the gross moist stability change with T_0 show considerable intermodel spread (Fig. 3a), although most values fall below the CC-implied rate. The clear-sky water vapor radiative feedback parameters also vary among models (Fig. 3b), but the moist radiative feedback strength r_{qm} appears consistently smaller than the dry radiative feedback strength r_{qd} . The cloud-radiative feedback parameter spans a range of positive values between 0.07 and 0.2 (Fig. 3c, left). Almost all models project a smaller r_c with increasing surface temperature (Fig. 3c, right), although the spread in the magnitude of this weakening is considerable.

6. Response to uniform warming in the AMIP mean parameter regime

The standard parameter regime for the simple process model is the multimodel mean of the 29 member AMIP ensemble. The parameter values for this regime are shown in Table 1, and the corresponding model solution is shown in Fig. 1c. To examine the response to uniform warming, the standard parameter regime is perturbed using values ranging from -10 to +10 K, as shown in Fig. 4a. In response to warming, the CWV field (Fig. 4b) moistens throughout the domain. This behavior is a result of parameterizing CWV using constant column relative humidity fractions (section 2e) and the CC relationship. Despite domain-wide moistening, the precipitating area contracts with warming. The ascent area fraction y_a also shows commensurate decreases with increasing T_0 (Fig. 4c). This decrease is accompanied by ascent area precipitation intensification (Fig. 4d).

This response of the simple process model to uniform warming is qualitatively similar to the narrowing-intensifying behavior of the ITCZ in observations (Wodzicki and Rapp 2016; Byrne et al. 2018; Su et al. 2020) and climate models (Lau and Kim 2015; Byrne and Schneider 2016b). The simple model even captures the warming-induced increase in ascent area strength and decrease in descent area strength (Fig. 4c; right axis) previously noted for climate models (Su et al. 2019). To isolate the physics controlling ascent area contraction with warming, we leverage the tight relationship between ascent and moist areas by examining the processes controlling moist area (y_m) fractional changes with warming. The linear approximation to y_m from (40) allows us to express the fractional change in y_m as the sum of five terms:

$$\delta_{ym} \approx \underbrace{C_{m0}\delta_{m0}}_{\text{gross moist stability}} - \underbrace{C_{rc}\delta_{rc}}_{\text{cloud radiative}} - \underbrace{C_{rd}\delta_{q0}}_{\text{dry radiative feedbacks}}$$

$$- \underbrace{C_{rm}\delta_{q0}}_{\text{moist radiative}} - \underbrace{C_{qd}\delta_{qd}}_{\text{poleward moisture}}, \qquad (49)$$

where $\delta_{ym} = (1/y_m)(dy_m/dT_0)$ (units of % K⁻¹). In (49), the contribution to δ_{ym} from each process is represented by a positive coefficient multiplying a fractional change. Terms δ_{q0} , δ_{qd} , δ_{rc} , and δ_{m0} are the fractional changes in q_0 , q_d , r_c , and m_0 respectively. Both δ_{q0} and δ_{qd} are given by the CC scaling at temperatures T_0 and T_d , respectively. Parameters γ_s and γ_q

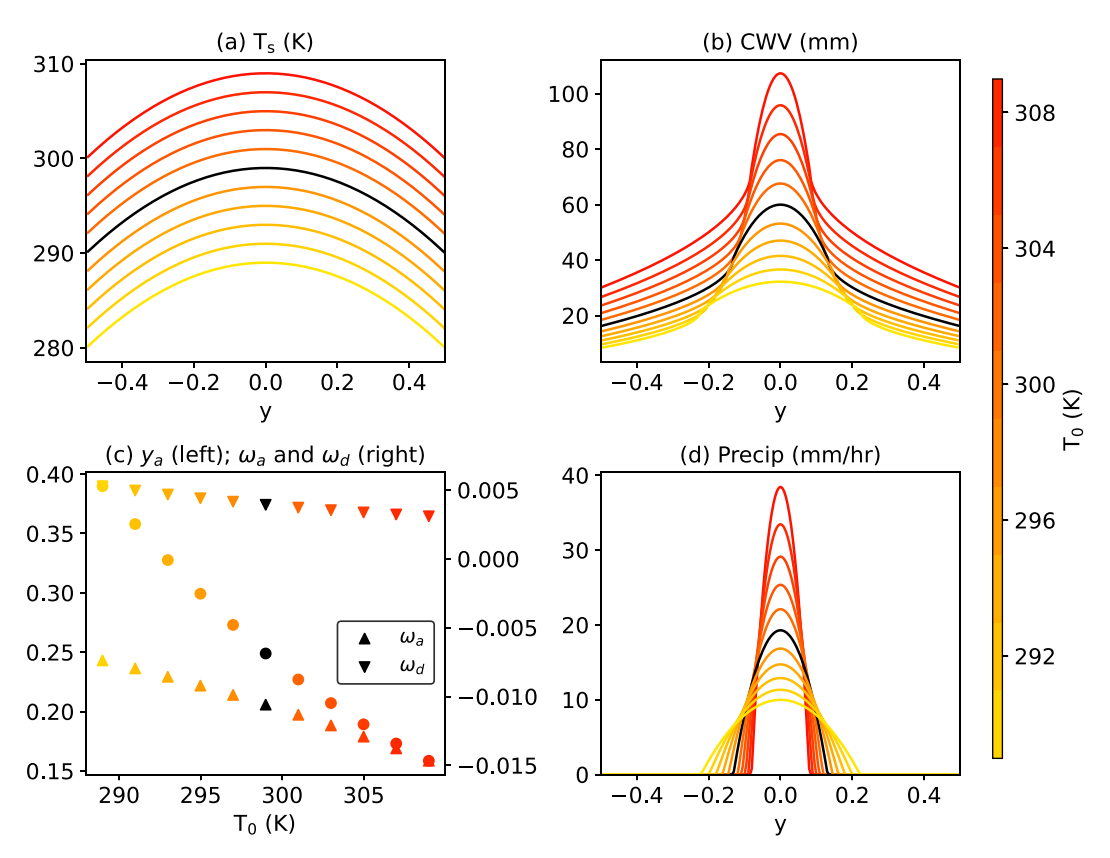


FIG. 4. Perturbations in (a) surface temperature T_0 , and the resulting simple model solutions for (b) CWV; (c) ascent area y_a (dots), ascent strength ω_a (upward pointing triangle), and descent strength ω_d (downward pointing triangle); and (d) precipitation. The units of ω_a and ω_d are $\times 10^{-3}$ Pa s⁻¹. Solutions with control parameter values from Table 1 are shown in black.

determine δ_{m0} , while γ_r determines δ_{rc} . The coefficients for water vapor radiative feedbacks in the dry and moist regimes are C_{rd} and C_{rm} , respectively. Similarly, C_{rc} , C_{m0} , and C_{qd} are the coefficients for contributions from cloud-radiative effects, gross moist stability effects, and the poleward moisture transport, respectively. Each coefficient is a nontrivial function of the model feedback parameters (shown in the supplemental material).

Figure 5 shows the numerically computed values of δ_{ya} and δ_{ym} , where $\delta_{ya} = (1/y_a)(dy_a/dT_0)$. The analytic approximation to δ_{ym} and its constituent effects are also shown. The analytic approximate value for δ_{ym} (-1% K⁻¹) obtained using (40) is close to the numerical value (-1.3% K⁻¹) obtained from (37). The fractional change in y_m receives noticeable contributions from four out of five terms in (49). The moist radiative feedback (-1.5% K⁻¹), the gross moist stability reduction with T_0 (-1.1% K⁻¹), and the poleward moisture transport (-1.5% K⁻¹) show comparable contributions to narrowing. The dry radiative feedback due to increased water vapor emission contributes to relatively weak narrowing (-0.3% K⁻¹). Weakening cloud-radiative feedbacks with increasing T_0 contributes to a moist area expansion of 3.4% K⁻¹. Increased atmospheric water vapor with warming is responsible for three out of the five effects in (49). Increased moisture enhances

both atmospheric cooling in the dry regime and atmospheric heating in the moist regime; increased moisture along the domain edge also increases poleward moisture transports, following the parameterization in (24).

A physical understanding of the various contributions to δ_{ym} is now sought by examining the controls on peak precipitation P_0 . Note that there are two constraints on P_0 . The first constraint is imposed by the local balance at y=0 and is given by

$$P_0 = \frac{E_0 + r_{qm}q_0 + F_0(1 - m)}{m_{\text{eff}}}. (50)$$

Expression (50) is obtained after rearranging (11) and using (21) and (30). The second constraint is imposed by the domain energy balance, and is given by

$$P_0 = \frac{3}{2(1+r_c)} \left[\frac{f_T - F_0}{y_m} - r_{qd} \beta_d \left(\frac{1-y_m}{y_m} \right) - r_{qm} \beta_m \right].$$
 (51)

Expression (51) results upon combining (25) and (26) and (31)–(34). This expression links P_0 to domain-mean quantities, and is a nonlocal constraint. An increase in P_0 due to changes to the right-hand side of (50) will be balanced by a y_m

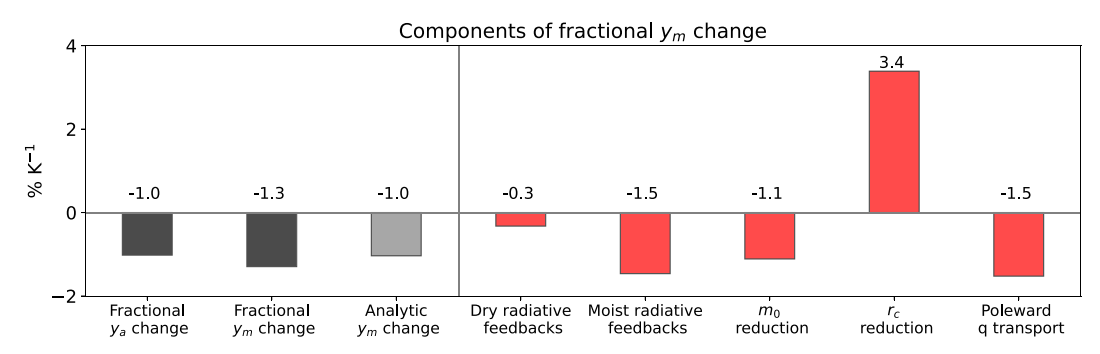


FIG. 5. The fractional y_a and y_m changes with T_0 are shown as black bars. The gray bar shows the fractional y_m change deduced from an analytic expression for y_m . The red bars denote contributions to the fractional y_m from the analytic expression.

decrease in (51) and vice versa. With this understanding of the P_0 – y_m relationship, the various contributions to δ_{ym} in Fig. 5 are examined:

- (i) Weaker cloud-radiative feedbacks and a smaller gross moist stability: under warming, the cloud-radiative effects weaken—presumably due to lesser high-cloud cover as discussed in section 5c—and the gross moist stability m_0 reduces due to large M_q changes. Both these changes impact the effective gross moist stability following (30), and thereby P_0 following (50). Weaker cloud-radiative effects reduce P_0 and increase y_m , while a smaller gross moist stability increases P_0 and reduces y_m .
- (ii) Stronger moist radiative feedbacks: the peak CWV value q_0 increases under warming. This increases the water vapor absorption at y = 0 as well as P_0 following (50) which leads to a moist area contraction following (51).
- (iii) Stronger dry radiative feedbacks and increased poleward moisture export: the dry regime CWV increases under warming, following (32) and (34), which in turn increases the dry regime emission. The poleward moisture transports increase due to a steeper moisture gradient at the domain boundaries. Both these effects lead to greater surface evaporation E_0 following (35), which implies a larger P_0 following (50) and therefore a smaller moist area.

In the simple model, the moist area fraction changes under warming therefore stem from the requirement to simultaneously satisfy both local and nonlocal constraints on precipitation.

7. Contributions to AMIP intermodel spread

In this section, we perturb the simple process model parameters according to the range of values seen in the AMIP ensemble. The perturbation experiments highlight the most sensitive parameters in the simple model, as well as parameters with most explanatory power for the intermodel spread within the AMIP ensemble.

a. Response to feedback parameters

Figure 6 shows results from a parameter perturbation experiment in which T_0 is kept fixed, while r_c , r_{qm} , and m_0 are

separately perturbed, using values from the 29 member AMIP ensemble. The responses in Fig. 6 suggest that increasing cloud-radiative and water vapor feedbacks, or reducing the gross moist stability narrows the ascent region, while intensifying the ascent area precipitation. In particular, the simple model appears remarkably sensitive to m_0 (Figs. 6e,f). Perturbing the other parameters according to their AMIP spread generates much smaller responses than seen in Fig. 6 (not shown). Figure 6 implies that the coupling between convection, circulation and radiation could be the key physical processes impacting climate model spread.

b. Synthetic ensemble to interrogate AMIP spread

In the simple process model, the ascent area properties are strongly sensitive to the cloud radiative feedback strength (Figs. 6a,b). However, we find that the spread in r_c does not explain the inter-AMIP-model spread in the ascent area fraction response to warming (not shown). Among other candidate parameters suggested by the simple process model, γ_s , γ_q , and r_{qm} are found to explain the most amount of AMIP intermodel spread. This is now illustrated by building a synthetic ensemble of simple models with the following attributes:

- (i) The synthetic ensemble has 29 members, corresponding to the number of AMIP models used. The synthetic ensemble is generated by letting the simple model take parameter values γ_s , γ_q and r_{qm} from each of the 29 AMIP models. All other parameters are fixed at the AMIP multimodel mean value (Table 1). In other words, the spread in the synthetic ensemble is largely generated by γ_s , γ_q , and r_{qm} differences among AMIP models.
- (ii) Each member of the synthetic ensemble is forced with a different spatially uniform surface temperature change. This change corresponds to the tropical mean temperature difference between the late (1997–2014) and early (1979–96) historical periods for each AMIP model. These values range between 0.23 and 0.44 K, with a median value of 0.29 K.
- (iii) Each member of the synthetic ensemble yields predictions for ascent area fraction and domain-mean precipitation changes (units of % K⁻¹) under uniform warming over the AMIP historical period.

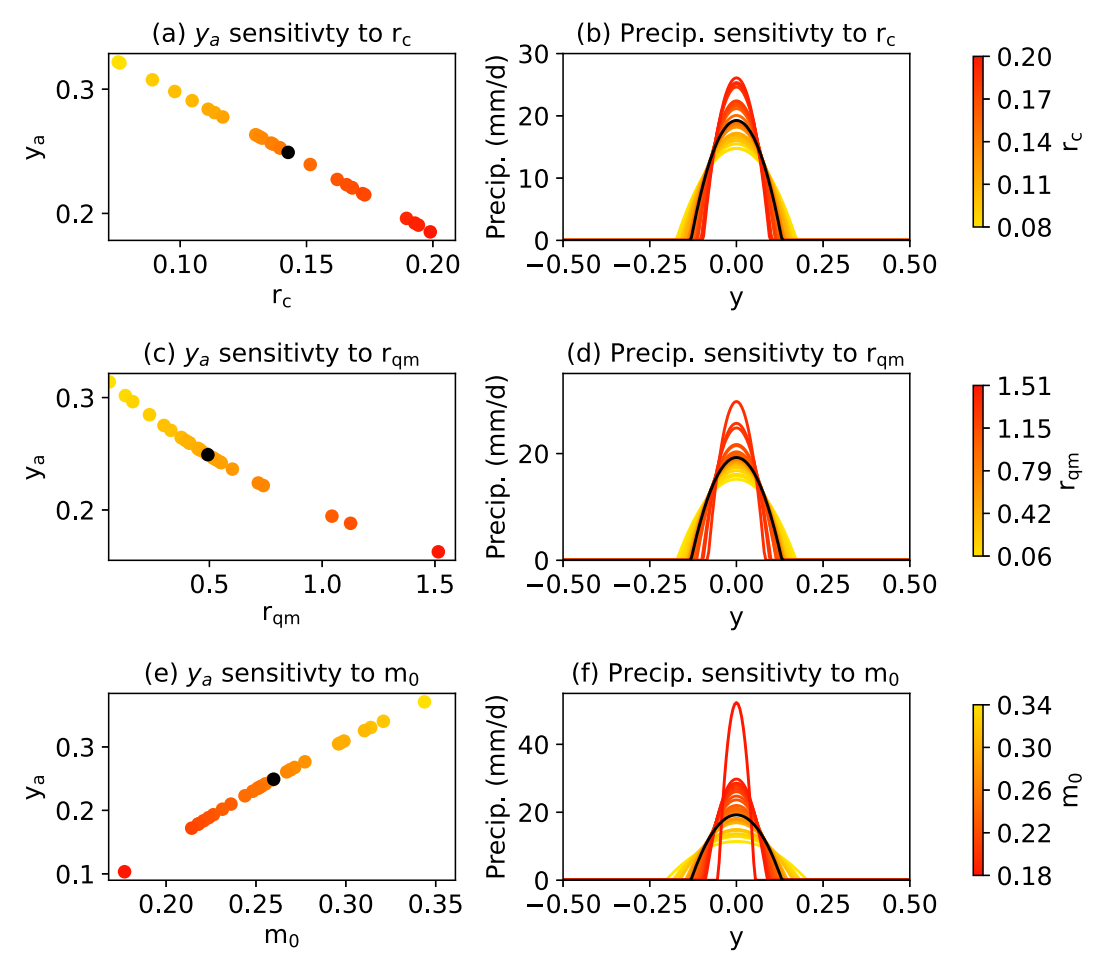


FIG. 6. Narrowing-intensifying ascent area in the simple model resulting from parameter perturbations in (a),(b) r_c , (c),(d) $r_{\rm qm}$, and (e),(f) m_0 . (left) Changes in y_a , and (right) the meridional profile of precipitation. The black colors indicate solutions using parameters from the reference regime. In each row, the color bar on the right depicts the range of perturbed values.

Relationships between the AMIP ensemble and the synthetic ensemble driven by γ_s , γ_q , and r_{qm} variations are now discussed.

The ascent area fraction in the AMIP models is defined as the fraction of tropics (35°N–35°S) with monthly mean $\omega_{500} < 0$. The ascent strength is measured using the average ω_{500} over the ascent area. Fractional changes (units of % K⁻¹) are computed using differences in surface temperature between the late and early historical periods. For each AMIP model, fractional changes in ascent area, domain mean precipitation, ascent strength and ascent area averaged precipitation are computed. These quantities serve as benchmarks against which we evaluate the simple process model.

Figure 7 compares the model spread generated by the synthetic ensemble (generated using γ_s , γ_q and r_{qm} variations) to that found in the AMIP ensemble. The spread in ascent area change (δ_{ya}) from the simple model is much larger than that found in the AMIP ensemble (Fig. 7a), with noticeable outliers. However, the ensemble means are comparable (\sim -1% K⁻¹ in the simple model and \sim -2% K⁻¹ in the AMIP ensemble).

The synthetic ensemble mean value also matches that estimated using the standard parameter regime in Fig. 5.

The global mean precipitation change per unit surface warming-termed the hydrological sensitivity-is an important measure of the hydrological cycle response to warming (Allen and Ingram 2002; Fläschner et al. 2016; Su et al. 2017). We compute a variant of this measure by only using the tropical domain in AMIP models, over a short time range spanning the late and early historical periods. This tropical hydrological sensitivity is also computed for each member of the synthetic ensemble generated by the simple model. The tropical hydrological sensitivities from the simple and AMIP model ensembles have similar spread (Fig. 7b). Although the AMIP ensemble mean lies below the 25th percentile of the synthetic ensemble, the two ensemble mean values are comparable $(\sim 2\% \text{ K}^{-1} \text{ for the simple model and } \sim 1.3\% \text{ K}^{-1} \text{ for the}$ AMIP ensemble). These values are noticeably smaller than the CC-implied rate of 7% K⁻¹ and close to the global hydrological cycle sensitivity estimate of 2% K⁻¹ (Held and Soden 2006). Much of the spread in both the ascent area fraction

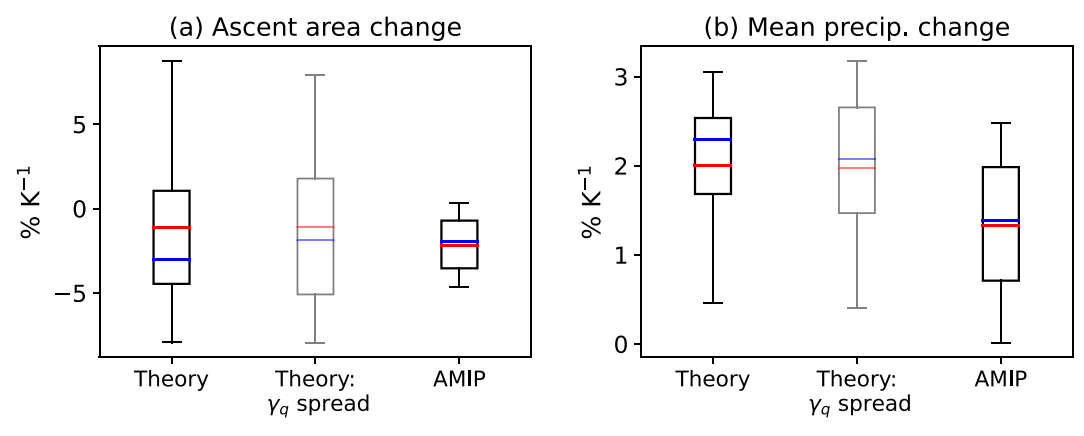


FIG. 7. The fractional (a) ascent area change and (b) domain-mean precipitation change expressed in units of % K^{-1} surface warming for both the simple model and the AMIP ensemble. The faded boxplot in both panels denotes the spread generated by varying γ_q alone. The boxes denote the interquartile range, and the whiskers denote the 5th and 95th percentiles. The red and the blue lines denote the mean and median, respectively.

change and the tropical hydrological sensitivity is recovered by perturbing γ_q alone. Excessive sensitivity to M_{q0} , and therefore m_0 , is a likely reason why the simple model generates a large spread in the ascent area fraction change (Fig. 7a).

Figure 8 shows that the spread generated by the synthetic ensemble is linearly correlated with the AMIP intermodel spread, with a correlation coefficient of \sim 0.46. This value is statistically significant at the 2.5% level. The ordinary least squares regression, which is sensitive to outliers, gives a slope of 1.58. The Huber regression slope (Huber 1992), which is less sensitive to outliers yields a slope closer to 1. Although considerable scatter exists on the scale of individual models in Fig. 8, the simple model proves skillful in identifying γ_s , γ_q , and r_{qm} as dominant sources of the inter-AMIP model spread. Three out of the 29 models analyzed show weak ascent area expansion instead of contraction. The simple model qualitatively captures this behavior, but overpredicts the expansion rate. In these three models, the ascent area expansion is

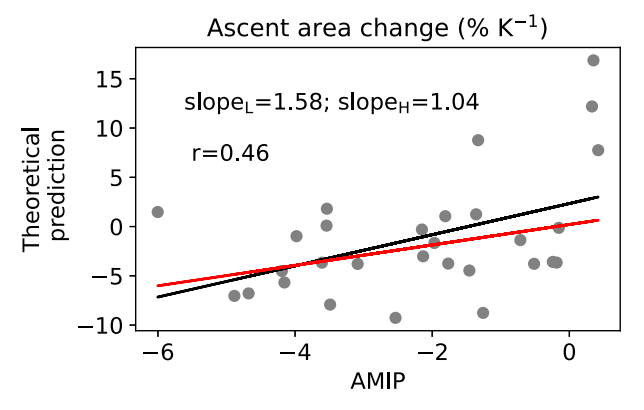


FIG. 8. Scatterplot between the fractional ascent area changes generated by the simple model (y axis) and AMIP models (x axis). The black line is the slope (slope $_L$) estimated using ordinary least squares regression. The red line is the slope (slope $_H$) estimated using Huber regression.

driven by *increases* in the gross moist stability with warming. This increase is due to stronger increases in M_{s0} compared to M_{q0} ($\gamma_s > \gamma_q$). A perturbation experiment that only varies γ_s and γ_q yields a correlation coefficient of ~0.36 between the synthetic and AMIP ensembles (not shown). This suggests that parameters controlling how M_{s0} and M_{q0} change with warming are significant contributors to spread. Examining the definitions of M_{s0} and M_{sq0} in (6) and (7), we deduce that processes controlling the vertical structures of ω , moisture and DSE, and their changes with warming are responsible for a reasonable fraction of the spread among AMIP models.

Figure 9 examines the relationships between the fractional changes in ascent area averaged precipitation (δ_{Pa}), and fractional changes in ascent area (δ_{ya}) and ascent strength ($\delta_{\omega a}$). As noted in Su et al. (2019), climate models display a strong inverse linear relationship between δ_{Pa} and δ_{va} (Fig. 9a), and a strong direct linear relationship between δ_{Pa} and $\delta_{\omega a}$ (Fig. 9b). These relationships are reproduced by the simple model (Figs. 9c,d). Quantitative differences do exist in the values of the regression slopes. Despite the greater spread in the simple model ensemble, the linear relationships appears to hold over the entire range of δ_{Pa} values in the synthetic ensemble (the inset in Figs. 9c and 9d). The inverse relationship between δ_{Pa} and δ_{ya} in Fig. 9c can be derived from (43) after neglecting fractional changes in domain-mean precipitation. The direct linear relationship between $\delta_{\omega a}$ and δ_{ya} in Fig. 9d follows from (46), upon neglecting fractional changes in M_{s0} and F_{ca} . The strong linear relationships noted in Figs. 9a and 9b, as well as in Su et al. (2019), therefore emerge from the leadingorder energetic constraints active over the ascent area. The competition between warming induced increases in gross dry stability and gross moisture stratification $(\gamma_s - \gamma_a)$ strongly determines both the ascent strength and area changes in the simple model (see supplemental material). Although the ascent strength among AMIP models mostly increases with warming, a few models do show decreasing ascent strength (Fig. 9b). In the synthetic ensemble, this behavior is reproduced (Fig. 9d)

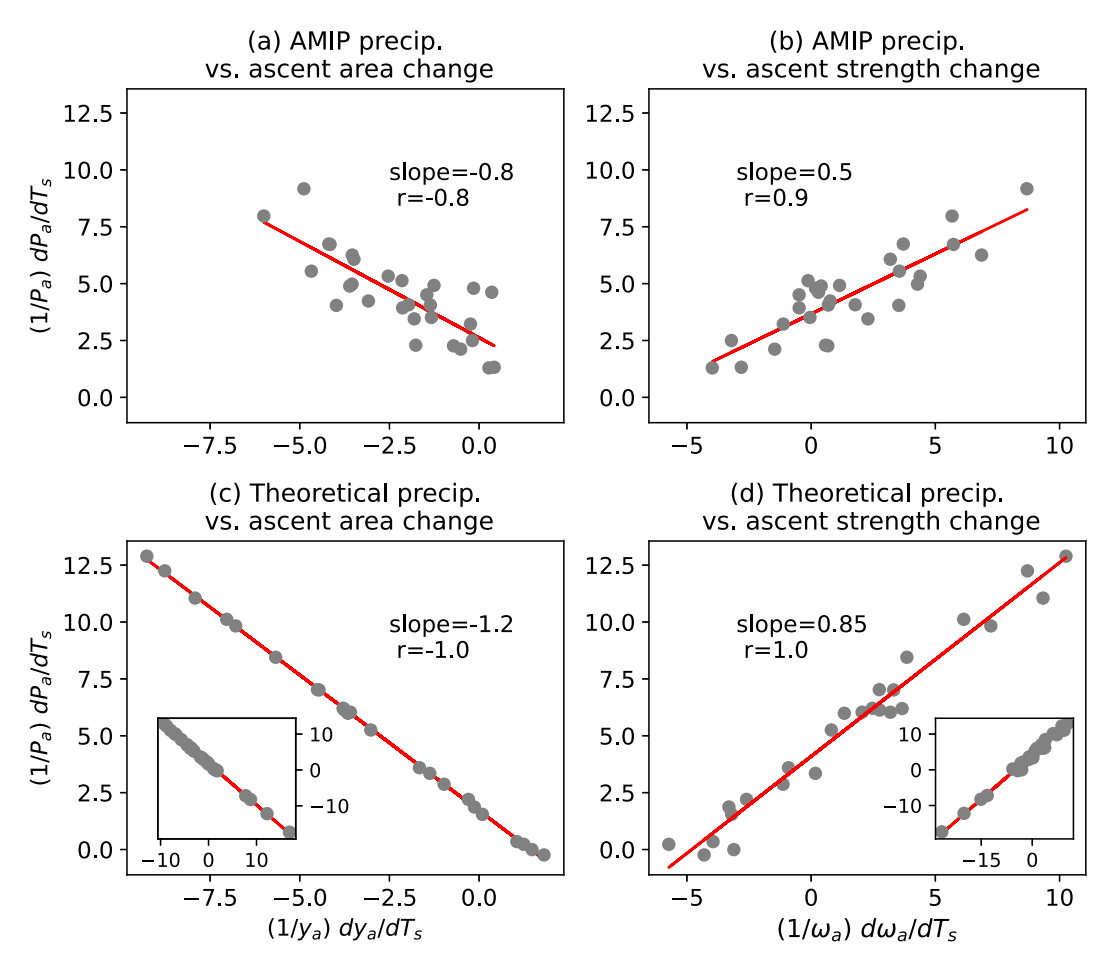


FIG. 9. The fractional changes in ascent area averaged precipitation regressed against (a),(c) fractional changes in ascent area and (b),(d) fractional changes in ascent strength. The relationships obtained from AMIP models in (a) and (b) are compared to those from the simple model in (c) and (d). The inset plots in the bottom row are zoomed out versions that include outlier models and consequently have larger axes ranges. All quantities have units of $\% K^{-1}$.

in parameter regimes with much stronger increases in the gross dry stability than the gross moisture stratification (see supplemental material).

8. Summary and discussion

a. Summary

A simple zonally symmetric model is constructed to study changes in ascent area fraction under global warming. An imposed meridional profile of surface temperature drives an overturning circulation in the model. A moist, precipitating regime is separated from a dry, nonprecipitating regime by a threshold value of column water vapor (CWV). Precipitation, cloud-radiative effects, and clear-sky radiative effects are all parameterized as functions of CWV. The clear-sky atmospheric cooling increases with increasing CWV in the dry regime, but decreases with increasing CWV in the moist regime. The area occupied by the ascending branch of the overturning circulation is calculated as an explicit function of the surface temperature and of parameters governing the cloud-radiative, clear-sky radiative, and moist convective feedbacks. These

parameters are estimated using 29 different AMIP models. The mean of the AMIP-estimated parameter values provides the standard parameter regime for the simple model.

The simple model predicts a narrowing of ascent area under uniform surface warming. An analytic expression for the ascent area allows a decomposition of the various effects contributing to ascent area changes. Under warming, the ascent area contracts due to reduced gross moist stability in the strongly ascending region, increased poleward moisture transports out of the domain, and increased water vapor absorption in moist regions and emission in dry regions. The ascent area expands due to weaker cloud-radiative effects with warming. The sum of these effects yields an ascent area contraction ${\sim}1\%~{\rm K}^{-1}$ in the simple model.

The simple model closely tracks the ensemble means for ascent area and domain-mean precipitation fractional changes, which is noteworthy since these constraints were not explicitly imposed. The simple model is used to interrogate the source of spread in AMIP model fractional ascent area changes. The simple model overpredicts the spread magnitude, but still explains $\sim 21\%$ of the inter model spread. A large portion of

this spread is attributed to spread in how the gross moisture stratification and gross dry stability change with warming. The simple model also obtains comparable values for the AMIP multimodel means in ascent area fraction and domain mean precipitation changes with warming. Previously reported ascent area relationships (Byrne and Schneider 2016a; Su et al. 2019; Schiro et al. 2019) are also reproduced in the simple model. These include a direct linear relationship between ascent strength and ascent area-averaged precipitation, and an inverse linear relationship between ascent area and ascent area-averaged precipitation. These results suggest that much of the physics associated with ascent area narrowing can be explained using energetics, circulation, and radiative feedbacks.

b. Condensing ITCZ width impacts

The simple model formulated here is closely related to the models of Bretherton and Sobel (2002), Peters and Bretherton (2005), and Bretherton et al. (2006). These studies simplify the Quasi-Equilibrium Tropical Circulation Model (QTCM; Neelin and Zeng 2000) using WTG and closed-domain approximations to study ascent area properties. Our model includes more realistic physics, which permits a comprehensive evaluation of the influences on the ascent area fraction, and helps connect to AMIP models. For instance, we have not assumed a closed domain; this accounts for the influence of energy export outside the domain on ascent area properties. Moreover, the effects of shortwave absorption in the moist regime—which are absent in the QTCM radiation scheme (Chou and Neelin 1996)—but potentially important for radiatively driven circulations (Voigt and Shaw 2015)—are included. A consequence of including shortwave absorption effects is that the clear-sky radiative feedbacks of water vapor have opposing effects in the moist and dry regimes (Beucler and Cronin 2016). Increased atmospheric water vapor increases atmospheric absorption in the moist region, but increases atmospheric emission in the dry region. These contrasting water vapor feedbacks quantitatively impact the ascent area narrowing rate under warming. The AMIP models suggest that the cloud-radiative feedback parameter (Su and Neelin 2002; Lin and Mapes 2004; Kim et al. 2015) is sensitive to the tropics-mean surface temperature, implying weaker cloud-radiative feedbacks with warming. This weakening is posited to occur because of lesser anvil detrainment from convective clouds (Bony et al. 2016), which in turn reduces longwave trapping per unit precipitation. Including this temperature dependence in the simple model contributes to ascent area expansion with warming (which are counteracted by other processes to yield net ascent area contraction).

An analytic expression for the ascent area fraction is used to decompose the warming induced ascent area contraction into five terms. Each of these terms is consistent with previously reported impacts on the ITCZ width. These impacts include cloud-radiative effects (Voigt and Shaw 2015; Dixit et al. 2018; Albern et al. 2018), water vapor feedbacks (Voigt and Shaw 2015), gross moist stability in the ascent area (Peters and Bretherton 2005; Byrne and Schneider 2016b) and the role of poleward moisture export (Byrne and Schneider 2016b). Additionally, increasing the

meridional surface temperature gradient also increases the poleward moisture transport, which leads to a narrower, intense ascent area. This result is consistent with Burls and Fedorov (2017) who note the impact of a changing SST gradient on the ITCZ width. The upped-ante mechanism (Neelin et al. 2003; Chou and Neelin 2004) does not explicitly appear in the simple expression derived here, but it operates implicitly. Ascent area narrowing in the simple model implies stronger moisture gradients and stronger inflow on the ascent area margins, and therefore stronger ventilation. The upped-ante mechanism therefore always produces more narrowing than would be seen in the absence of ventilation, but this mechanism is set in motion by other parametric changes.

c. Process-level understanding in climate models

Explicit expressions for the ascent area fraction help identify simple model parameters critical to a process-oriented understanding of ascent area contraction. Although the simple model parameters are idealized representations of more complex physics, they prove useful in highlighting climate model development targets. Among AMIP models, the changing gross moist stability in heavily precipitating regions is identified as an important source of spread. This gross moist stability in turn depends on vertical structures of MSE and vertical velocities, and particularly on the competing influences between column moistening and tropopause height increases (Yu et al. 1998; Chou and Neelin 2004; Chou et al. 2013b). The results here motivate future work examining how the gross moist stability in ascent regions would change under warming. Although the AMIP analysis in this study suggests a small decrease in ascent-region gross moist stability with warming, several modeling studies suggest an increase (Byrne and Schneider 2016b; Wills et al. 2017; Neogi and Singh 2022). Addressing this discrepancy requires tighter observational bounds on gross moist stability using satellite (Inoue and Back 2017) and field campaign (Inoue and Back 2015; Raymond and Fuchs-Stone 2021) data. Additional constraints, particularly for behavior under warming, could be provided by storm-resolving simulations (Wing et al. 2018; Stevens et al. 2019).

d. Future extensions

The simple process model tracks ascent area properties in complex climate models despite lacking features such as zonal asymmetry in the SST forcing, land—ocean contrasts, and detailed parameterizations for convection and radiation. One useful extension of the model would be explicitly including zonal asymmetries to understand the role of SST pattern effect (Dong et al. 2019; Seager et al. 2019) on the tropical ascent area fraction as outlined in section 4c. Another would be incorporating the downstream effects of ITCZ narrowing on the overall Hadley cell extent through its influence on angular momentum transports (Watt-Meyer and Frierson 2019; Hill et al. 2022). Stronger connections between mock overturning circulation models with moist physics and dry angular momentum conserving models

would serve to refine theories for both the ascent area fraction and Hadley cell width.

Acknowledgments. This work was supported in part by Department of Energy Grant DE-SC0021312 (FA, JDN, and HS) and National Science Foundation Grants AGS-2123327 (SAH) and AGS-1936810 (JDN). Insightful reviews from Andrea Jenney and Zhiming Kuang helped improve this manuscript.

Data availability statement. The AMIP model data were obtained from https://esgf-node. llnl.gov/projects/esgf-llnl/. The ERA5 data are available at https://doi.org/10.24381/cds.bd0915c6. The GPCP data are available from https://psl.noaa.gov/data/gridded/data.gpcp.html.

REFERENCES

- Adames, Á. F., and D. Kim, 2016: The MJO as a dispersive, convectively coupled moisture wave: Theory and observations. *J. Atmos. Sci.*, 73, 913–941, https://doi.org/10.1175/JAS-D-15-0170.1.
- Ahmed, F., 2021: The MJO on the equatorial beta plane: An eastward-propagating Rossby wave induced by meridional moisture advection. J. Atmos. Sci., 78, 3115–3135, https://doi. org/10.1175/JAS-D-21-0071.1.
- —, and C. Schumacher, 2015: Convective and stratiform components of the precipitation-moisture relationship. *Geophys. Res. Lett.*, 42, 10453–10462, https://doi.org/10.1002/2015GL066957.
- —, and J. D. Neelin, 2019: Explaining scales and statistics of tropical precipitation clusters with a stochastic model. *J. Atmos. Sci.*, 76, 3063–3087, https://doi.org/10.1175/JAS-D-18-0368.1.
- —, Á. F. Adames, and J. D. Neelin, 2020: Deep convective adjustment of temperature and moisture. *J. Atmos. Sci.*, 77, 2163–2186, https://doi.org/10.1175/JAS-D-19-0227.1.
- Albern, N., A. Voigt, S. A. Buehler, and V. Grützun, 2018: Robust and nonrobust impacts of atmospheric cloud-radiative interactions on the tropical circulation and its response to surface warming. *Geophys. Res. Lett.*, 45, 8577–8585, https://doi. org/10.1029/2018GL079599.
- Allen, M. R., and W. J. Ingram, 2002: Constraints on future changes in climate and the hydrologic cycle. *Nature*, 419, 228–232, https://doi.org/10.1038/nature01092a.
- Armour, K. C., N. Siler, A. Donohoe, and G. H. Roe, 2019: Meridional atmospheric heat transport constrained by energetics and mediated by large-scale diffusion. *J. Climate*, 32, 3655–3680, https://doi.org/10.1175/JCLI-D-18-0563.1.
- Beucler, T., and T. W. Cronin, 2016: Moisture-radiative cooling instability. J. Adv. Model. Earth Syst., 8, 1620–1640, https:// doi.org/10.1002/2016MS000763.
- Bjerknes, J., 1938: Saturated-adiabatic ascent of air through dryadiabatically descending environment. *Quart. J. Roy. Meteor.* Soc., 64, 325–330.
- Bony, S., B. Stevens, D. Coppin, T. Becker, K. A. Reed, A. Voigt, and B. Medeiros, 2016: Thermodynamic control of anvil cloud amount. *Proc. Natl. Acad. Sci. USA*, 113, 8927–8932, https://doi.org/10.1073/pnas.1601472113.
- Bretherton, C. S., 1987: A theory for nonprecipitating moist convection between two parallel plates. Part I: Thermodynamics and "linear" solutions. *J. Atmos. Sci.*, **44**, 1809–1827, https://doi.org/10.1175/1520-0469(1987)044<1809:ATFNMC>2.0.CO;2.

- —, and A. H. Sobel, 2002: A simple model of a convectively coupled walker circulation using the weak temperature gradient approximation. *J. Climate*, 15, 2907–2920, https://doi.org/10.1175/1520-0442(2002)015<2907:ASMOAC>2.0.CO;2.
- —, M. E. Peters, and L. E. Back, 2004: Relationships between water vapor path and precipitation over the tropical oceans. J. Climate, 17, 1517–1528, https://doi.org/10.1175/1520-0442(2004)017<1517:RBWVPA>2.0.CO;2.
- —, P. N. Blossey, and M. Khairoutdinov, 2005: An energy-balance analysis of deep convective self-aggregation above uniform SST. J. Atmos. Sci., 62, 4273–4292, https://doi.org/10.1175/JAS3614.1.
- —, and M. E. Peters, 2006: Interpretation of simple and cloud-resolving simulations of moist convection–radiation interaction with a mock-walker circulation. *Theor. Comput. Fluid Dyn.*, **20**, 421–442, https://doi.org/10.1007/s00162-006-0029-7.
- Burls, N. J., and A. V. Fedorov, 2017: Wetter subtropics in a warmer world: Contrasting past and future hydrological cycles. *Proc. Natl. Acad. Sci. USA*, 114, 12888–12893, https:// doi.org/10.1073/pnas.1703421114.
- Byrne, M. P., and T. Schneider, 2016a: Energetic constraints on the width of the intertropical convergence zone. *J. Climate*, **29**, 4709–4721, https://doi.org/10.1175/JCLI-D-15-0767.1.
- —, and —, 2016b: Narrowing of the ITCZ in a warming climate: Physical mechanisms. *Geophys. Res. Lett.*, 43, 11350–11357, https://doi.org/10.1002/2016GL070396.
- —, A. G. Pendergrass, A. D. Rapp, and K. R. Wodzicki, 2018: Response of the intertropical convergence zone to climate change: Location, width, and strength. *Curr. Climate Change Rep.*, **4**, 355–370, https://doi.org/10.1007/s40641-018-0110-5.
- Chou, C., and J. D. Neelin, 1996: Linearization of a longwave radiation scheme for intermediate tropical atmospheric models. J. Geophys. Res., 101, 15129–15145, https://doi.org/10.1029/96JD01015.
- —, and —, 2004: Mechanisms of global warming impacts on regional tropical precipitation. *J. Climate*, 17, 2688–2701, https://doi.org/10.1175/1520-0442(2004)017<2688:MOGWIO>2.0.CO;2.
- —, J. C. Chiang, C.-W. Lan, C.-H. Chung, Y.-C. Liao, and C.-J. Lee, 2013a: Increase in the range between wet and dry season precipitation. *Nat. Geosci.*, 6, 263–267, https://doi.org/10.1038/ngeo1744.
- —, T.-C. Wu, and P.-H. Tan, 2013b: Changes in gross moist stability in the tropics under global warming. *Climate Dyn.*, 41, 2481–2496, https://doi.org/10.1007/s00382-013-1703-2.
- DeAngelis, A. M., X. Qu, M. D. Zelinka, and A. Hall, 2015: An observational radiative constraint on hydrologic cycle intensification. *Nature*, 528, 249–253, https://doi.org/10.1038/nature15770.
- Dixit, V., O. Geoffroy, and S. C. Sherwood, 2018: Control of ITCZ width by low-level radiative heating from upper-level clouds in aquaplanet simulations. *Geophys. Res. Lett.*, 45, 5788–5797, https://doi.org/10.1029/2018GL078292.
- Dong, Y., C. Proistosescu, K. C. Armour, and D. S. Battisti, 2019: Attributing historical and future evolution of radiative feed-backs to regional warming patterns using a Green's function approach: The preeminence of the western Pacific. *J. Climate*, 32, 5471–5491, https://doi.org/10.1175/JCLI-D-18-0843.1.
- Donohoe, A., K. C. Armour, A. G. Pendergrass, and D. S. Battisti, 2014: Shortwave and longwave radiative contributions to global warming under increasing CO₂. *Proc. Natl. Acad. Sci. USA*, 111, 16700–16705, https://doi.org/10.1073/pnas.1412190111.
- —, A. R. Atwood, and M. P. Byrne, 2019: Controls on the width of tropical precipitation and its contraction under

- global warming. *Geophys. Res. Lett.*, **46**, 9958–9967, https://doi.org/10.1029/2019GL082969.
- Emanuel, K., 2019: Inferences from simple models of slow, convectively coupled processes. *J. Atmos. Sci.*, 76, 195–208, https://doi.org/10.1175/JAS-D-18-0090.1.
- —, A. A. Wing, and E. M. Vincent, 2014: Radiative-convective instability. J. Adv. Model. Earth Syst., 6, 75–90, https://doi.org/10.1002/2013MS000270.
- Emanuel, K. A., J. David Neelin, and C. S. Bretherton, 1994: On large-scale circulations in convecting atmospheres. *Quart. J. Roy. Meteor. Soc.*, 120, 1111–1143, https://doi.org/10.1002/qj. 49712051902.
- Eyring, V., S. Bony, G. A. Meehl, C. A. Senior, B. Stevens, R. J. Stouffer, and K. E. Taylor, 2016: Overview of the Coupled Model Intercomparison Project phase 6 (CMIP6) experimental design and organization. *Geosci. Model Dev.*, 9, 1937–1958, https://doi.org/10.5194/gmd-9-1937-2016.
- Fläschner, D., T. Mauritsen, and B. Stevens, 2016: Understanding the intermodel spread in global-mean hydrological sensitivity. J. Climate, 29, 801–817, https://doi.org/10.1175/JCLI-D-15-0351.1.
- Frierson, D. M., I. M. Held, and P. Zurita-Gotor, 2007: A gray-radiation aquaplanet moist GCM. Part II: Energy transports in altered climates. J. Atmos. Sci., 64, 1680–1693, https://doi.org/10.1175/JAS3913.1.
- Harrop, B. E., and D. L. Hartmann, 2016: The role of cloud radiative heating within the atmosphere on the high cloud amount and top-of-atmosphere cloud radiative effect. *J. Adv. Model. Earth* Syst., 8, 1391–1410, https://doi.org/10.1002/2016MS000670.
- Held, I. M., and A. Y. Hou, 1980: Nonlinear axially symmetric circulations in a nearly inviscid atmosphere. J. Atmos. Sci., 37, 515–533, https://doi.org/10.1175/1520-0469(1980)037<0515: NASCIA>2.0.CO;2.
- —, and B. J. Soden, 2006: Robust responses of the hydrological cycle to global warming. *J. Climate*, **19**, 5686–5699, https://doi. org/10.1175/JCLI3990.1.
- Hersbach, H., and Coauthors, 2020: The ERA5 global reanalysis. *Quart. J. Roy. Meteor. Soc.*, **146**, 1999–2049, https://doi.org/10.1002/qj.3803.
- Hill, S. A., S. Bordoni, and J. L. Mitchell, 2022: A theory for the Hadley cell descending and ascending edges throughout the annual cycle. *J. Atmos. Sci.*, 79, 2515–2528, https://doi.org/10. 1175/JAS-D-21-0328.1.
- Huber, P. J., 1992: Robust estimation of a location parameter. *Breakthroughs in Statistics*, Springer, 492–518.
- Huffman, G. J., and Coauthors, 1997: The Global Precipitation Climatology Project (GPCP) combined precipitation dataset. Bull. Amer. Meteor. Soc., 78, 5–20, https://doi.org/10.1175/ 1520-0477(1997)078<0005:TGPCPG>2.0.CO;2.
- Hwang, Y.-T., and D. M. Frierson, 2010: Increasing atmospheric poleward energy transport with global warming. *Geophys. Res. Lett.*, 37, L24807, https://doi.org/10.1029/2010GL045440.
- Inoue, K., and L. E. Back, 2015: Gross moist stability assessment during TOGA COARE: Various interpretations of gross moist stability. *J. Atmos. Sci.*, 72, 4148–4166, https://doi.org/ 10.1175/JAS-D-15-0092.1.
- —, and —, 2017: Gross moist stability analysis: Assessment of satellite-based products in the GMS plane. *J. Atmos. Sci.*, **74**, 1819–1837, https://doi.org/10.1175/JAS-D-16-0218.1.
- Jenney, A. M., D. A. Randall, and M. Branson, 2020: Understanding the response of tropical ascent to warming using an energy balance framework. J. Adv. Model. Earth Syst., 12, e2020MS002056, https://doi.org/10.1029/2020MS002056.

- Kim, D., M.-S. Ahn, I.-S. Kang, and A. D. Del Genio, 2015: Role of longwave cloud–radiation feedback in the simulation of the Madden–Julian oscillation. *J. Climate*, 28, 6979–6994, https:// doi.org/10.1175/JCLJ-D-14-00767.1.
- Knutti, R., M. A. Rugenstein, and G. C. Hegerl, 2017: Beyond equilibrium climate sensitivity. *Nat. Geosci.*, 10, 727–736, https://doi.org/10.1038/ngeo3017.
- Kuang, Z., 2012: Weakly forced mock Walker cells. J. Atmos. Sci., 69, 2759–2786, https://doi.org/10.1175/JAS-D-11-0307.1.
- Kuo, Y.-H., J. D. Neelin, and C. R. Mechoso, 2017: Tropical convective transition statistics and causality in the water vapor–precipitation relation. *J. Atmos. Sci.*, 74, 915–931, https://doi.org/10.1175/JAS-D-16-0182.1.
- Lau, W. K., and K.-M. Kim, 2015: Robust Hadley circulation changes and increasing global dryness due to CO₂ warming from CMIP5 model projections. *Proc. Natl. Acad. Sci. USA*, 112, 3630–3635, https://doi.org/10.1073/pnas.1418682112.
- Lin, J.-L., and B. E. Mapes, 2004: Radiation budget of the tropical intraseasonal oscillation. *J. Atmos. Sci.*, **61**, 2050–2062, https://doi. org/10.1175/1520-0469(2004)061<2050:RBOTTI>2.0.CO;2.
- Neelin, J. D., and I. M. Held, 1987: Modeling tropical convergence based on the moist static energy budget. *Mon. Wea. Rev.*, 115, 3–12, https://doi.org/10.1175/1520-0493(1987)115<0003: MTCBOT>2.0.CO;2.
- —, and J.-Y. Yu, 1994: Modes of tropical variability under convective adjustment and the Madden–Julian oscillation. Part I: Analytical theory. *J. Atmos. Sci.*, **51**, 1876–1894, https://doi.org/10.1175/1520-0469(1994)051<1876:MOTVUC>2.0.CO;2.
- —, and N. Zeng, 2000: A quasi-equilibrium tropical circulation model—Formulation. J. Atmos. Sci., 57, 1741–1766, https://doi. org/10.1175/1520-0469(2000)057<1741:AQETCM>2.0.CO;2.
- —, C. Chou, and H. Su, 2003: Tropical drought regions in global warming and El Niño teleconnections. *Geophys. Res. Lett.*, 30, 2275, https://doi.org/10.1029/2003GL018625.
- —, M. Münnich, H. Su, J. E. Meyerson, and C. E. Holloway, 2006: Tropical drying trends in global warming models and observations. *Proc. Natl. Acad. Sci. USA*, **103**, 6110–6115, https://doi.org/10.1073/pnas.0601798103.
- —, O. Peters, and K. Hales, 2009: The transition to strong convection. J. Atmos. Sci., 66, 2367–2384, https://doi.org/10.1175/2009JAS2962.1.
- Neogi, S., and M. S. Singh, 2022: Understanding changes in the tropical circulation under global warming using a cloud resolving model and a conceptual model. *J. Climate*, 35, 5855– 5868, https://doi.org/10.1175/JCLI-D-21-0854.1.
- North, G. R., 1975: Theory of energy-balance climate models. *J. Atmos. Sci.*, **32**, 2033–2043, https://doi.org/10.1175/1520-0469 (1975)032<2033:TOEBCM>2.0.CO;2.
- Paynter, D., and V. Ramaswamy, 2014: Investigating the impact of the shortwave water vapor continuum upon climate simulations using GFDL global models. *J. Geophys. Res. Atmos.*, 119, 10720–10737, https://doi.org/10.1002/2014JD021881.
- Pendergrass, A. G., and D. L. Hartmann, 2014: The atmospheric energy constraint on global-mean precipitation change. *J. Cli*mate, 27, 757–768, https://doi.org/10.1175/JCLI-D-13-00163.1.
- Peters, M. E., and C. S. Bretherton, 2005: A simplified model of the Walker circulation with an interactive ocean mixed layer and cloud-radiative feedbacks. *J. Climate*, 18, 4216–4234, https://doi.org/10.1175/JCLI3534.1.
- Pierrehumbert, R. T., 1995: Thermostats, radiator fins, and the local runaway greenhouse. *J. Atmos. Sci.*, **52**, 1784–1806, https://doi.org/10.1175/1520-0469(1995)052<1784:TRFATL>2.0.CO:2.

- Polvani, L. M., and A. H. Sobel, 2002: The Hadley circulation and the weak temperature gradient approximation. *J. Atmos. Sci.*, **59**, 1744–1752, https://doi.org/10.1175/1520-0469(2002)059<1744: THCATW>2.0.CO;2.
- Raymond, D. J., 1994: Convective processes and tropical atmospheric circulations. *Quart. J. Roy. Meteor. Soc.*, 120, 1431–1455, https://doi.org/10.1002/qj.49712052002.
- —, and Ž. Fuchs-Stone, 2021: Emergent properties of convection in OTREC and predict. *J. Geophys. Res. Atmos.*, 126, e2020JD033585, https://doi.org/10.1029/2020JD033585.
- —, S. L. Sessions, A. H. Sobel, and Ž. Fuchs, 2009: The mechanics of gross moist stability. *J. Adv. Model. Earth Syst.*, **1**, e2020JD033585, https://doi.org/10.3894/JAMES.2009.1.9.
- Sahany, S., J. D. Neelin, K. Hales, and R. B. Neale, 2014: Deep convective transition characteristics in the Community Climate System Model and changes under global warming. *J. Climate*, 27, 9214–9232, https://doi.org/10.1175/JCLI-D-13-00747.1.
- Schiro, K. A., J. D. Neelin, D. K. Adams, and B. R. Lintner, 2016: Deep convection and column water vapor over tropical land versus tropical ocean: A comparison between the amazon and the tropical western Pacific. J. Atmos. Sci., 73, 4043–4063, https://doi.org/10.1175/JAS-D-16-0119.1.
- ——, H. Su, Y. Wang, B. Langenbrunner, J. H. Jiang, and J. D. Neelin, 2019: Relationships between tropical ascent and high cloud fraction changes with warming revealed by perturbation physics experiments in cam5. *Geophys. Res. Lett.*, 46, 10112–10121, https://doi.org/10.1029/2019GL083026.
- —, and Coauthors, 2022: Model spread in tropical low cloud feedback tied to overturning circulation response to warming. *Nat. Commun.*, 13, 7119, https://doi.org/10.1038/s41467-022-34787-4.
- Seager, R., M. Cane, N. Henderson, D.-E. Lee, R. Abernathey, and H. Zhang, 2019: Strengthening tropical Pacific zonal sea surface temperature gradient consistent with rising greenhouse gases. *Nat. Climate Change*, 9, 517–522, https://doi.org/ 10.1038/s41558-019-0505-x.
- Sherwood, S., and Coauthors, 2020: An assessment of Earth's climate sensitivity using multiple lines of evidence. *Rev. Geophys.*, 58, e2019RG000678, https://doi.org/10.1029/2019RG000678.
- Siler, N., G. H. Roe, and K. C. Armour, 2018: Insights into the zonal-mean response of the hydrologic cycle to global warming from a diffusive energy balance model. *J. Climate*, 31, 7481–7493, https://doi.org/10.1175/JCLI-D-18-0081.1.
- Sobel, A. H., and C. S. Bretherton, 2000: Modeling tropical precipitation in a single column. *J. Climate*, **13**, 4378–4392, https://doi.org/10.1175/1520-0442(2000)013<4378:MTPIAS>2.0.CO;2.
- —, and J. D. Neelin, 2006: The boundary layer contribution to intertropical convergence zones in the quasi-equilibrium tropical circulation model framework. *Theor. Comput. Fluid Dyn.*, 20, 323–350, https://doi.org/10.1007/s00162-006-0033-y.
- —, J. Nilsson, and L. M. Polvani, 2001: The weak temperature gradient approximation and balanced tropical moisture waves. J. Atmos. Sci., 58, 3650–3665, https://doi.org/10.1175/1520-0469(2001)058<3650:TWTGAA>2.0.CO;2.
- Stevens, B., and Coauthors, 2019: Dyamond: The dynamics of the atmospheric general circulation modeled on non-hydrostatic domains. *Prog. Earth Planet. Sci.*, 6, 61, https://doi.org/10. 1186/s40645-019-0304-z.

- Su, H., and J. D. Neelin, 2002: Teleconnection mechanisms for tropical Pacific descent anomalies during El Niño. *J. Atmos. Sci.*, **59**, 2694–2712, https://doi.org/10.1175/1520-0469(2002)059<2694: TMFTPD>2.0.CO;2.
- —, and Coauthors, 2017: Tightening of tropical ascent and high clouds key to precipitation change in a warmer climate. *Nat. Commun.*, 8, 15771, https://doi.org/10.1038/ncomms15771.
- —, C. Zhai, J. H. Jiang, L. Wu, J. D. Neelin, and Y. L. Yung, 2019: A dichotomy between model responses of tropical ascent and descent to surface warming. *npj Climate Atmos. Sci.*, 2, 8, https://doi.org/10.1038/s41612-019-0066-8.
- —, L. Wu, C. Zhai, J. H. Jiang, J. D. Neelin, and Y. L. Yung, 2020: Observed tightening of tropical ascent in recent decades and linkage to regional precipitation changes. *Geophys. Res. Lett.*, 47, e2019GL085809, https://doi.org/10.1029/2019GL085809.
- Trenberth, K. E., and D. P. Stepaniak, 2003: Seamless poleward atmospheric energy transports and implications for the Hadley circulation. *J. Climate*, **16**, 3706–3722, https://doi.org/10.1175/1520-0442(2003)016<3706:SPAETA>2.0.CO;2.
- Voigt, A., and T. A. Shaw, 2015: Circulation response to warming shaped by radiative changes of clouds and water vapour. *Nat. Geosci.*, 8, 102–106, https://doi.org/10.1038/ngeo2345.
- Watt-Meyer, O., and D. M. Frierson, 2019: ITCZ width controls on Hadley cell extent and eddy-driven jet position and their response to warming. J. Climate, 32, 1151–1166, https://doi. org/10.1175/JCLI-D-18-0434.1.
- Wills, R. C., X. J. Levine, and T. Schneider, 2017: Local energetic constraints on Walker circulation strength. J. Atmos. Sci., 74, 1907–1922, https://doi.org/10.1175/JAS-D-16-0219.1.
- Wing, A. A., K. A. Reed, M. Satoh, B. Stevens, S. Bony, and T. Ohno, 2018: Radiative–convective equilibrium model inter-comparison project. *Geosci. Model Dev.*, 11, 793–813, https://doi.org/10.5194/gmd-11-793-2018.
- Wodzicki, K., and A. Rapp, 2016: Long-term characterization of the Pacific ITCZ using TRMM, GPCP, and ERA-Interim. J. Geophys. Res. Atmos., 121, 3153–3170, https://doi.org/10.1002/ 2015JD024458.
- Wofsy, J., and Z. Kuang, 2012: Cloud-resolving model simulations and a simple model of an idealized Walker cell. *J. Climate*, **25**, 8090–8107, https://doi.org/10.1175/JCLI-D-11-00692.1.
- Wolding, B., J. Dias, G. Kiladis, F. Ahmed, S. W. Powell, E. Maloney, and M. Branson, 2020: Interactions between moisture and tropical convection. Part I: The coevolution of moisture and convection. J. Atmos. Sci., 77, 1783–1799, https://doi.org/10.1175/JAS-D-19-0225.1.
- Wood, R., and C. S. Bretherton, 2006: On the relationship between stratiform low cloud cover and lower-tropospheric stability. J. Climate, 19, 6425–6432, https://doi.org/10.1175/JCLI3988.1.
- Yu, J.-Y., C. Chou, and J. D. Neelin, 1998: Estimating the gross moist stability of the tropical atmosphere. *J. Atmos. Sci.*, 55, 1354–1372, https://doi.org/10.1175/1520-0469(1998)055<1354: ETGMSO>2.0.CO:2.
- Zhou, W., S.-P. Xie, and D. Yang, 2019: Enhanced equatorial warming causes deep-tropical contraction and subtropical monsoon shift. *Nat. Climate Change*, **9**, 834–839, https://doi.org/10.1038/s41558-019-0603-9.



Supplemental Material

Journal of Climate

A Process Model for ITCZ Narrowing under Warming Highlights Clear-Sky Water Vapor Feedbacks and Gross Moist Stability Changes in AMIP Models https://doi.org/10.1175/JCLI-D-22-0689.1

© Copyright 2023 American Meteorological Society (AMS)

For permission to reuse any portion of this work, please contact permissions@ametsoc.org. Any use of material in this work that is determined to be "fair use" under Section 107 of the U.S. Copyright Act (17 USC §107) or that satisfies the conditions specified in Section 108 of the U.S. Copyright Act (17 USC §108) does not require AMS's permission. Republication, systematic reproduction, posting in electronic form, such as on a website or in a searchable database, or other uses of this material, except as exempted by the above statement, requires written permission or a license from AMS. All AMS journals and monograph publications are registered with the Copyright Clearance Center (https://www.copyright.com). Additional details are provided in the AMS Copyright Policy statement, available on the AMS website (https://www.ametsoc.org/PUBSCopyrightPolicy).

Supplemental information: "A process model for ITCZ narrowing under warming highlights clear-sky water vapor feedbacks and gross moist stability changes in AMIP models"

N.B. the figures in this supplementary material are prefixed with the letter S. Referents without a prefix denote figures and tables in the main text.

1 Fractional change in y_m

Using $y_m \sim -C_2/C_1$ from (37), we can write:

$$\frac{1}{y_m}\frac{dy_m}{dT_0} = \delta_{ym} = \frac{1}{C_1}\frac{dC_1}{dT_0} - \frac{1}{C_2}\frac{dC_2}{dT_0}.$$
 (S1)

Using the definitions of C_1 and C_2 from (38) and (39) respectively, we can write:

$$\delta_{ym} \approx r_{qd} \Delta_d q_0^* \left(\frac{(1 + Nm_{\text{eff}})}{r_{qd} \beta_d - f_h - r_{qm} q_0 + m_{\text{eff}} (F_0 + r_{qm} q_0 - NR_q)} + \frac{1}{[f_T - F_0 - r_{qd} \beta_d]} \right) \delta_0$$

$$- r_{qm} q_0^* \left(\frac{r_0 (1 - m_{\text{eff}}) + Nm_{\text{eff}} (r_{in} + \Delta_m)}{r_{qd} \beta_d - f_h - r_{qm} q_0 + m_{\text{eff}} (F_0 + r_{qm} q_0 - NR_q)} \right) \delta_0$$

$$- \frac{r_c}{C_1} \left[\frac{(f_h + r_{qm} q_0 - r_{qd} \beta_d) (1 - m_0)}{m_{\text{eff}}} - f_q \right] \delta_{rc}$$

$$+ \left[\frac{(f_h + r_{qm} q_0 - r_{qd} \beta_d) m_0 (1 + r_c)}{[r_{qd} \beta_d - f_h - r_{qm} q_0 + m_{\text{eff}} (F_0 + r_{qm} q_0 - NR_q)] m_{\text{eff}}} \right] \delta_{m0}$$

$$- \left(\frac{f_q (1 + r_c)}{C_1} q_d^* \delta_e \right), \quad (S2)$$

where

$$\delta_0 = \frac{1}{q_0} \frac{dq_0}{dT_0}$$
 and $\delta_e = \frac{1}{q_d} \frac{dq_d}{dT_0}$

are the fractional changes in q_0 and q_d respectively. Similarly, δ_{rc} and δ_{m0} are the fractional changes in r_c and m_0 respectively. In (S2), $N=\frac{3}{2}$ and

$$\Delta_d = \left(\frac{r_{in} + 2r_e}{3}\right) q_0^* \tag{S3}$$

$$\Delta_m = \frac{2[r_0 - r_{in}]}{3} q_0^*.$$
 (S4)

In (S3) and (S4), r_0 and r_{in} are the column saturation fractions for the region of peak ascent (y = 0) and the moist-dry interface ($|y| = y_m/2$) respectively. The saturation column water vapor at y = 0 is q_0^* . Matching the expression in (S2) to (48), we get:

$$C_{rd} = r_{qd} \Delta_d q_0^* \left(\frac{(1 + Nm_{\text{eff}})}{r_{qd} \beta_d - f_h - r_{qm} q_0 + m_{\text{eff}} (F_0 + r_{qm} q_0 - NR_q)} + \frac{1}{f_T - F_0 - r_{qd} \beta_d} \right)$$
 (S5)

$$C_{rm} = r_{qm} q_0^* \left(\frac{r_0 (1 - m_{\text{eff}}) + N m_{\text{eff}} (r_{in} + \Delta_m)}{r_{qd} \beta_d - f_h - r_{qm} q_0 + m_{\text{eff}} (F_0 + r_{qm} q_0 - N R_q)} \right)$$
 (S6)

$$C_{rc} = \frac{r_c}{C_1} \left[\frac{(f_h + r_{qm}q_0 - r_{qd}\beta_d)(1 - m_0)}{m_{\text{eff}}} - f_q \right]$$
(S7)

$$C_{m0} = \frac{(f_h + r_{qm}q_0 - r_{qd}\beta_d) m_0 (1 + r_c)}{m_{\text{eff}} [r_{qd}\beta_d - f_h - r_{qm}q_0 + m_{\text{eff}} (F_0 + r_{qm}q_0 - NR_q)]}$$
(S8)

$$C_{qd} = \frac{f_q(1+r_c)}{C_1}q_d^*$$
 (S9)

2 Horizontal scale of the CWV field

2.1 Moist and dry regime scales

In Section 2e, the meridional shape of the CWV profiles was partly specified using (16). Alternatively, the CWV shape can be deduced from the governing equations. Although this route provides a solution that is not analytically tractable, the dominant controls on the CWV scale can be still be understood. Following Section 2c, we consider the following vertical structures for the horizontal wind \mathbf{v} and the vertical velocity ω :

$$\mathbf{v}(y,p) = v_1(y)V(p) \tag{S10}$$

$$\omega(y,p) = \omega_1(y)\Omega(p) \tag{S11}$$

$$q(y) = q_1(y)\langle b \rangle \tag{S12}$$

where V(p), $\Omega(p)$ and b(p) are the vertical structures of the horizontal wind, vertical velocity and the specific humidity respectively. In (S15), $\langle b \rangle$ is the vertical integral of the b. The continuity equation gives the following relations:

$$\omega_1 = \partial_{\nu} v_1 \tag{S13}$$

$$V(p) = \partial_p \Omega(p), \tag{S14}$$

where in (S13), we have used the fact that zonal symmetry does not permit zonal wind divergence. Using (S10)–(S14) in (1) and (2) respectively gives:

$$-v_1 \frac{dq_1}{dy} M_{qp} + \omega_1 q_1 M_{qp} = E - P \tag{S15}$$

$$-\omega_1 M_s = P + F_c, \tag{S16}$$

where

$$M_{qp} = \langle \Omega \frac{db}{dp} \rangle = -\langle Vb \rangle$$

and M_s is defined as in (6). Combining (S15) and (S16) gives:

$$v_1 \frac{dq_1}{dy} M_{qp} - \omega_1 M_{qp} q_1 = -[E + F_c + \omega_1 M_s],$$
 (S17)

where the parameterization for F_c from (19) has been used.

2.1.1 Complete solution

We derive expressions for ω_1 and v_1 using (S15) and (S13) respectively:

$$\omega_1(y) = -\frac{P + F_c}{M_s} \tag{S18}$$

$$v_1(y) = -\int_0^y \omega_1(y')dy' = \int_0^y \frac{(P + F_c)}{M_s} dy',$$
 (S19)

where (S18) has been used in deriving (S19).

Now substituting (S18) and (S19) in (S17), we have:

$$\left(\int_{0}^{y} \frac{(P+F_{c})}{M_{s}} dy'\right) \frac{dq_{1}}{dy} M_{qp} + (P+F_{c}) \frac{M_{qp}}{M_{s}} q_{1} = P - E.$$
 (S20)

Terms P and F_c in (S20) can themselves be expressed in terms of q_1 using (19), (25) and (26). Moreover (35) is used to substitute for E. These substitutions into (S20) yield an **integro-differential equation**, which when solved will produce a complete solution for q_1 in terms of the other feedback parameters. However, this solution for q_1 is not analytically tracatable and is therefore not pursued here.

2.1.2 Simplified solution

Since (S20) is too complex to delve into physical insights, we simplify the problem to gain some understanding of the the dominant controls on the CWV scale. The expression in (S15) is separately solved for the ascent and descent regions, within each of which we assume slowly varying values for ω_1 , v_1 , F_c and E (assumed constant with y). This procedure yields the following solution for the moist regime:

$$q(y) = \exp\left(\frac{\omega_1}{v_1}y\right) \left[q_0 + \hat{b} \int_0^y \frac{P - E}{v_1 M_{qp}} \exp\left(-\frac{\omega_1}{v_1}y'\right) dy'\right]$$
 (S21)

and the following for the dry regime:

$$q = q_{in} \exp\left(\frac{\omega_1}{v_1} \left[y - \frac{y_m}{2} \right] \right) - \exp\left(\frac{\omega_1}{v_1} y\right) \hat{b} \int_{y_m/2}^{y} \frac{E}{v_1 M_{qp}} \exp\left(-\frac{\omega_1}{v_1} y'\right) dy', \tag{S22}$$

where $q=q_0$ at y=0 and $q=q_{in}$ at $y=y_m/2$. In both (S21) and (S22), the CWV decay scale is governed by the term ω_1/v_1 . Physically, ω_1/v_1 measures the strength of the divergent circulation. A stronger circulation (larger ω_1/v_1) creates stronger moisture gradients—deduced from steeper decay in (S21) and (S22). Note that this term is negative in the ascent region and positive in the descent region. Accordingly, the decay is exponential in the moist regime—from (S21)—and slower than exponential in the dry regime—from (S22). The latter is due to the competing effects of the exponential growth in the first right hand side term of (S21) and exponential decay in the second right hand side term. Overall, this analysis suggests that the meridional profile of CWV is governed by interactions with the dynamics (and not simply set by the surface).

3 Ascent area properties

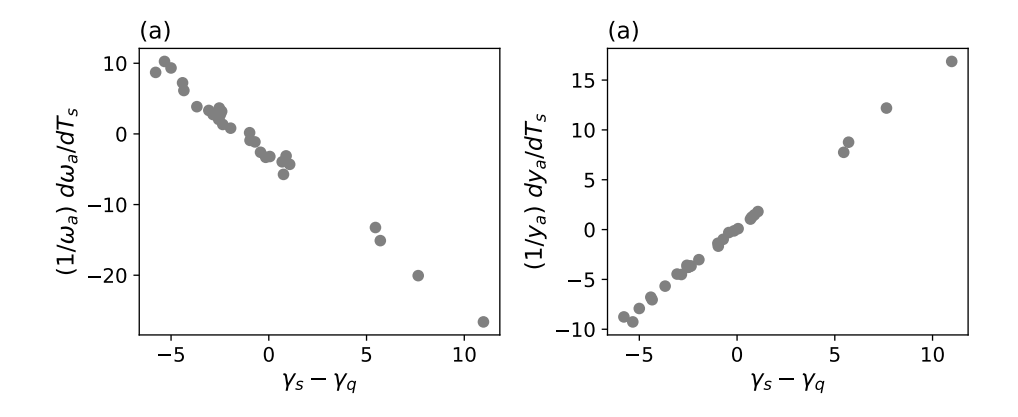


Figure S1: (a) Scatter plot between the fractional ascent area strength (y axis) and $\gamma_s - \gamma_q$ (x axis) generated by the simple model. (b) As in (a) but for the fractional ascent area change in the y-axis.

Figure S1 shows that much of the scatter in the ascent area properties from Fig. 9 is determined by the difference between γ_s and γ_q seen in the various models. In the synthetic ensemble, a larger gross dry stability increase compared to a gross moisture stratification results in weakening ascent strength (Fig. S1a), and smaller ascent area contraction or even expansion (Fig. S1b).

4 Analysis of AMIP Models

A list of 29 AMIP models were used in the study, as shown in Table S1.

Table S1: List of 29 AMIP Models used in the study along with their institutions, nominal horizontal resolution and the ascent area fraction computed as described in Section 7. In the rightmost column, models that show ascent area expansion with warming are indicated in blue.

Model	Institution	Nominal Resolution (km)	Ascent area fraction change (%K ⁻¹)
ACCESS-CM2	CSIRO-ARCCSS	250	-2.0
BCC-CSM2-MR	BCC	100	-1.5
BCC-ESM1	BCC	250	-2.2
CESM2	NCAR	100	0.4
CESM2-WACCM	NCAR	100	-3.6
CESM2-WACCM-FV2	NCAR	250	-6.0
CMCC-CM2-HR4	CMCC	100	-0.2
CMCC-CM2-SR5	CMCC	100	-1.4
CNRM-CM6-1	CNRM-CERFACS	250	-0.5
CNRM-CM6-1-HR	CNRM-CERFACS	50	-0.2
CNRM-ESM2-1	CNRM-CERFACS	250	-0.7
CanESM5	CCCma	500	-1.8
EC-Earth3	EC-Earth-Consortium	100	-4.0
EC-Earth3-AerChem	EC-Earth-Consortium	100	-3.1
EC-Earth3-Veg	EC-Earth-Consortium	100	-4.2
FGOALS-f3-L	CAS	100	-1.3
FGOALS-g3	CAS	250	0.4
HadGEM3-GC31-LL	МОНС	250	-1.8
HadGEM3-GC31-MM	MOHC	100	-3.5
INM-CM5-0	INM	100	-0.2
IPSL-CM6A-LR	IPSL	250	-3.5
KIOST-ESM	KIOST	250	0.3
MIROC6	MIROC	250	-3.5
MPI-ESM-1-2-HAM	HAMMOZ-Consortium	250	-4.7
MPI-ESM1-2-HR	MPI-M	100	-4.2
MPI-ESM1-2-LR	MPI-M	250	-4.9
MRI-ESM2-0	MRI	100	-2.1
NorCPM1	NCC	250	-1.3
UKESM1-0-LL	МОНС	250	-2.5

These models were chosen based on the availability of the following monthly mean fields: precipitation (pr), surface skin temperature (ts), all-sky (rlut, rsdt, rsut, rlds, rlus, rsds, rsus) and clear-sky (rlutcs, rsutcs, rldscs, rsuscs) radiative fluxes, surface sensible (hfss) and latent heat (hfls) fluxes, and vertical profiles of specific humidity (hus), temperature (ta), geopotential (Z) and vertical velocity (wap). These fields are required for the parameter estimation in Section 5 as well as for comparisons to the simple model in Section 7.